Technical University of Berlin
Faculty I Humanities and Educational Sciences
Institute for Speech and Communication
Audio Communication Group

Master's thesis in the program
"Audio Communication and Technology" (M. Sc.)

Adjoint-Based Monopole Synthesis of Sound Sources with Complex Directivities

Arne Birk Hölter

July 2020

Supervision:
Prof. Dr. Stefan Weinzierl
Dr.-Ing. Mathias Lemke
Dr. rer. nat. Florian Straube

Abstract

Numerical time domain methods are continuously improving and gain in importance in virtual acoustics. The accurate modeling of directive sound sources is a prerequisite for acoustical simulations. In contrast to frequency domain methods, the directivity pattern of sound sources cannot be analytically implemented in the time domain directly. The sound sources are rather approximated by the superposition of monopoles around the directive sound source. For that purpose, an adjoint-based monopole synthesis method is discretized in a finite differences time domain (FDTD) scheme. Therein, the full non-linear Euler equations are solved by means of computational aeroacoustics (CAA).
To efficiently compute reference sound fields, an analytical complex directivity point source (CDPS) model is embedded into the existing architecture of the CAA solver, which enables a decomposition of the computing domain to parallelize the computation. In order to avoid unfavorable interferences between the monopoles in FDTD, its spatial expansion is analyzed. Finally the adjoint-based monopole synthesis method is considered for a dipole, a quadrupole and a (complex) circular piston model. The results are evaluated by graphical representations and technical measures, e.g., 3D directivity pattern figures. The analysis is not only limited to the reproduction of the reference directivity patterns, as it is as well the intention of this thesis to examine the procedure of the adjoint-based monopole synthesis method.

Zusammenfassung

Numerische Methoden im Zeitbereich sind ein aktiver Forschungsbereich in der virtuellen Akustik. Die Modellierung von richtungsabhängigen Schallquellen ist eine Vorraussetzung für akustische Simulationen. Im Gegensatz zu den Methoden im Frequenzbereich können Richtcharakteristiken von Schallquellen nicht direkt analytisch im Zeitbereich implementiert werden. Vielmehr werden die Schallquellen durch eine Superposition von Monopolen um die richtungsabhängige Schallquelle approximiert. Zu diesem Zweck wird eine adjungierten-basierte Monopolsynthese mithilfe eines finite Differenzenschema im Zeitbereich (FDTD) diskretisiert. Darin werden die kompletten nicht-linearen Euler Gleichungen mittels numerischer Strömungsakustik (CAA) gelöst.
Zur effizienten Berechnung von Referenzschallfeldern wird ein analytisches *Complex Directivity Point Source* (CDPS) Modell in die bestehende Architektur des CAA Lösers eingebettet, die eine Zerlegung des Rechengebiets zur Parallelisierung der Rechnungen ermöglicht. Um unerwünschte Interferenzen zwischen den Monopolen in FDTD zu vermeiden, wird die räumliche Ausdehnung der Monopole untersucht. Abschließend wird die adjungierten-basierte Monopolsynthese für einen Dipol, einen Quadrupol und einen (komplexen) Rundkolbenstrahler (*Circular Piston*) angewendet. Die Ergebnisse werden mittels graphischer Darstellung und technischer Beurteilungen, wie beispielsweise 3D Abbildungen von Richtcharakteristiken, ausgewertet. Die Analyse ist nicht nur auf die Nachbildung der Richtcharakteristiken beschränkt, sondern konzentriert sich auch auf die Vorgehensweise der adjungierten-basierten Monopolsynthese.

Contents

List of Figures

List of Tables

List of Symbols

	Symbol	Definition
Latin		
	A	governing operator
	c	speed of sound
	D	driving function of a sound source
	E	Euler equations
	f	frequency
	f_{c}	cut-off frequency
	f_{s}	sampling frequency
	f_{in}	input / test signal
	$\mathbf{g}$	geometric weight
	$G_{0,\mathsf{3D}}$	3D Green's function, free field acoustic transfer function
	H	directivity pattern
	j	imaginary unit, $\mathsf{j}^2 = -1$
	J	objective function
	K	phase scaling parameter of the complex circular piston
	l	transition length of the objective area mask function
	l_{s}	source expansion diameter
	L_p	sound pressure level
	M_{mol}	molar mass
	p	pressure field in the time domain
	p_0	ambient pressure
	p'	sound pressure
	p^*	adjoint pressure
	P_{ATF}	sound pressure transfer function in the frequency domain
	P	sound field in the frequency domain (complex frequency spectrum)
	$\mathbf{q}$	system state

Symbol	Definition
$\mathbf{q}^*$	adjoint system state
r_0	distance from the source to the receiver position, $\|\mathbf{x} - \mathbf{x_0}\|$
r_{in}	effective start of the objective area mask function
r_{out}	effective end of the objective area mask function
r_{s}	source region radius
R	gas constant
R_{s}	specific gas constant
$\mathbf{s}$	source term
s_{f}	source forcing signal
s_{g}	Gaussian distribution for the spatial source activation
s_p	source term regarding the pressure
t	time
T	total time
T_0	reference temperature
u_{tot}	total velocity, consists of $\|u\| + c$
$\mathbf{x}$	discretized computation area (grid), consists of the three spatial directions $[x_1, x_2, x_3]^{\mathsf{T}}$
$\mathbf{x_0}$	reference sound source location
$\mathbf{x_g}$	number of the discretized grid node
$\mathbf{x_{s,m}}$	optimized sound source locations

Symbol	Definition
Greek	
α	active radiating factor (ARF)
α_{s}	line search step width
β	angle from the source to the receiver, contains the azimuth φ and the elevation ϑ
γ	isentropic exponent
λ	wavelength
Λ_y	height of the loudspeaker
φ	azimuth angle
Ψ	mask function of the source region
ϱ_0	reference density of the air
σ	evaluation mask function
σ_{sd}	standard deviation
ϑ	elevation angle
Θ	radius of the circular piston

1 Introduction

To improve the acoustical behaviour of environments such as rooms, concert venues etc., acoustical optimizations are unavoidable. In most cases experimental optimizations are expensive and very time-consuming. The refined way is to apply acoustical simulations.
Acoustical simulations have been broadly developed and studied in the recent years, where mainly two categories of simulation methods have been formed: geometrical- and wave-based methods. Geometrical-based methods assume the sound propagation as a ray, while wave-based methods numerically approximate the solution of the wave equation (Takeuchi et al., 2019). Both allow a prediction of sound fields in a specific area emitted by any number of sound sources and receiver positions. To approximate real environments, such as rooms or open air venues, the actual simulation strategies still come up against limiting factors, e.g., the implementation of boundary conditions or non-uniform flow (Stein et al., 2019). Among these limiting factors, directive sound sources have to be highlighted as this thesis will be focused on them. Currently, in frequency domain approaches the frequency-dependent directivity is already considered, e.g., in the complex directivity point source (CDPS) model (Meyer, 1984; Feistel et al., 2009) or at least with simple source directivities in geometrical room acoustic simulations (Poirier-Quinot et al., 2017). For the most common time domain approaches, that mostly make use of finite difference time domain (FDTD) schemes, no method is available to date that is able to model complex directivities in an adequate way (see Sec. 1.1), i.e., directivity pattern impulse responses with changing amplitude and phase in terms of direction and frequency (Takeuchi et al., 2019).
More general, directivity means that different sound pressure amplitudes and phases are obtained in different directions on equidistant evaluation positions around the source, i.e., on a spherical surface with the source at the origin. If a sound field cannot be considered as diffuse, the obtained sound field is strongly influenced by directive sound sources. Therefore an implementation method of directive sound sources in FDTD is in need.
This thesis makes use of an adjoint-based approach which is able to solve the full non-linear Euler equations and the corresponding adjoint in the time domain by means of computa-

tional aeroacoustic (CAA) techniques (see Sec. 2). Stein et al. (2019) demonstrated that the method is able to optimize driving functions of sound sources. Moreover, the ability of the method to find optimal monopole source locations and the corresponding monopole weights to reconstruct directive sound sources will be analyzed.

1.1 State of the Art

The reproduction of sound sources with 3D audio systems in the frequency domain is well described in the literature, e.g., Wave Field Synthesis (WFS) or Near Field Compensated Higher Order Ambisonics (NFC - HOA) (Berkhout et al., 1992; de Vries et al., 1994; Slavik and Weinzierl, 2008; Ahrens, 2012). Usually, the sound sources are inserted as monopoles, i.e., point sources, because they are easily implemented and they may be described analytically well.

The complex directivity point source (CDPS) model is an analytical method to compute sound field predictions in the free field and the frequency domain (Meyer, 1984; van Beuningen and Start, 2000; Meyer and Schwenke, 2003; Feistel et al., 2009). Further, the model is able to deal with modeled and measured loudspeaker directivity data (Straube, 2019). The sound field is separately computed for every considered frequency in the CDPS model.

As the available computational power is increasing significantly in the recent time, time domain approaches become increasingly important. In this thesis a CAA method in a FDTD scheme is considered. It is based on the wave equation in the time domain instead of the Helmholtz equation. If the wave equation is expanded to the full non-linear Euler equations, an easier treatment of, i.a., non-uniform flow, boundary conditions and heat stratifications is possible (Stein et al., 2019). Instead of the complex directivity in the frequency domain approaches, the directivity is up to date modeled as a decomposition of the source into spatially located monopoles.

Source modeling in FDTD has already approached with many different methods. In general two different modeling strategies have been mainly considered: superposition of point sound sources and expansion into spherical harmonics or multipoles (Takeuchi et al., 2019).

First, the superposition of point sound sources approximates the directive source with secondary sources in the frequency domain. Subsequently, a set of appropriate coefficients must be determined for the predefined point sources (Redlich, 2017; Opdam et al., 2016), which may be solved, e.g., through the least-squares-method (Escolano et al., 2007). However, these methods must convert the results into the time domain, which may degrade the final accuracy.
Spherical-harmonics- or multipole-based methods consider the directivity in the time domain directly (Takeuchi et al., 2019). In the spherical-harmonics-based method a spatial Gaussian pulse is multiplied with the spherical harmonics, which approximates the desired directivity (Sakamoto and Takahashi, 2013). The method was already fitted to measured loudspeaker data in the work of Bilbao et al. (2019). The multipole-based method uses spatial derivatives of Dirac delta functions to express a desired directivity by their linear combination (Bilbao and Hamilton, 2018). The mentioned time domain methods do not consider frequency-wise directivity because they consider the directional pattern for all frequencies simultaneously.
Thus, no method exists which is able to control (time-directional) frequency-wise directivity and can be implemented directly in the time domain (Takeuchi et al., 2019).

1.2 Objective

Recent research has shown that the numerical time domain methods are continuously improving and gain in importance in acoustics as well as in the research area of virtual acoustics. As outlined above, the implementation of directive sound sources is still an active research area. A novel grid-based monopole synthesis approach was presented by Stein et al. (2020) using an adjoint-based CAA method which will be applied in this thesis too. It treats all grid nodes in a specific source region as monopole sources, which can be activated if necessary. But the method does not provide information of the activation process of the multiple monopoles directly. In contrast to the work of Stein et al. (2020), this thesis aims at synthesizing the directive sound source by adding gradually single monopoles in a predefined source region. Also, the objective of this procedure is to understand the optimization process of the adjoint-based monopole synthesis approach. Thus, directive sound sources shall be synthesized by a small number of monopole sources providing a result in the optimal sense.

The following sections are divided as follows: Sec. 2 highlights the implemented complex directivity point source (CDPS) model as well as the adjoint-based CAA method. Ensuing, Sec. 3 describes the simulation settings and the general setup of both methods. After documenting the computational tools, Sec. 4 gives an overview of the evaluation and visualization methods. The evaluated results and the discussion of the regarded testcases are given in Sec. 5. Finally, Sec. 6 compares the findings with the study of Stein et al. (2020) and draws a conclusion of the intended adjoint-based monopole synthesis method.

2 Methods

As described in Sec. 1, this thesis will focus on the implementation of directive sound sources in a FDTD scheme. To achieve this, an adjoint-based time domain method will be considered. An analytical sound field simulation which is based on the complex directivity point source (CDPS) model will serve as a reference for the validation during the CAA computation and in the post-processing.

2.1 Complex Directivity Point Source Model

The analytic CDPS model is widely used for sound field prediction in virtual acoustics, sound reproduction and sound reinforcement. It models sound sources as point sources, i.e., the loudspeakers' acoustical centers, with a complex directivity in the frequency domain. Subsequently, the propagation of all sources is computed and the produced partial sound pressure fields are added.

Formulated in equations, the fundamental equation of the CDPS model (Meyer, 1984, Eq. (5)); (van Beuningen and Start, 2000, Eq. (3-5)); (Meyer and Schwenke, 2003, Sec. 1.1); (Feistel et al., 2009, Eq. (11)) reads

$$P_{\mathsf{ATF}}(\mathbf{x},\omega) = \sum_{m=1}^{M} \left(H\left(\beta(\mathbf{x},\mathbf{x_{0,m}}),\omega\right) \circ G_{0,\mathsf{3D}}(\mathbf{x},\mathbf{x_{0,m}},\omega)\right) D(\mathbf{x_{0,m}},\omega), \tag{1}$$

where $H\left(\beta(\mathbf{x},\mathbf{x_{0,m}}),\omega\right)$ are the directivity patterns of the loudspeakers with $\beta(\mathbf{x},\mathbf{x_{0,m}})$ as the angle from the source position $\mathbf{x_{0,m}}$ to the receiver positions $\mathbf{x}$, i.e., to all discretized grid nodes in the three spatial directions x_1, x_2 and x_3, at the angular frequencies ω. Note that β contains both spherical angles, the azimuth φ and the elevation ϑ. $G_{0,\mathsf{3D}}(\mathbf{x},\mathbf{x_{0,m}},\omega)$ denotes the three dimensional free space Green's function, i.e., the ideal point source (Williams, 1999, Eq. (8.41), p. 265) and $\circ$ is the Hadamard product, i.e., element-wise matrix multiplication. $D(\mathbf{x_{0,m}},\omega)$ are the loudspeakers' driving functions and the output $P_{\mathsf{ATF}}(\mathbf{x},\omega)$ is the sound pressure transfer function at the receiver position $\mathbf{x}$ at the angular frequency ω.

As this thesis aims to reconstruct directivity patterns, the driving functions of the loudspeakers $D(\mathbf{x_{0,m}}, \omega)$ will be considered as uniformly driven sources

$$D(\mathbf{x_{0,m}}, \omega) = 1 \qquad \forall m \text{ and } \forall \omega. \tag{2}$$

Since the adjoint-based CAA solver is a time domain solver, the output $P_{\mathsf{ATF}}(\mathbf{x}, \omega)$ of the CDPS model has to be transformed into the time domain using an inverse discrete (fast) Fourier transform

$$p'(\mathbf{x}, t) = \mathcal{F}_t^{-1}(P_{\mathsf{ATF}}(\mathbf{x}, \omega)) \tag{3}$$

and is excited by a sound signal $f_{\mathsf{in}}(t)$ at every receiver position $\mathbf{x}$

$$p'_{\mathsf{out}}(\mathbf{x}, t) = p'(\mathbf{x}, t) *_t f_{\mathsf{in}}(t), \tag{4}$$

whereby the asterisk $*_t$ denotes the convolution with respect to time.

2.1.1 Directivity Pattern

First, variations of analytic directivity patterns $H\left(\beta(\mathbf{x}, \mathbf{x_{0,m}}), \omega\right)$ in the frequency domain are considered in this section. They characterize the generated reference sound field in the free field. Subsequently, the reference sound field is reproduced by a direct implementation in the time domain using the adjoint-based monopole synthesis method (see Sec. 2.2).

The variations range from simple directivity patterns as monopoles, dipoles and quadrupoles to more complex directivity patterns like the baffled circular piston model. The dipole and quadrupole will only be described by cosine functions. If an implementation of multipoles of a higher order is required—the dipole has the order 1 and the quadrupole the order 2—a spherical harmonics representation is recommended (Ahrens, 2012, Sec. 2).

The simple and not frequency dependent directivity patterns may be described as follows: the monopole radiates to all directions with the same amplitude. Since only the directivity is of interest, it reads

$$H_{\text{mono}}\left(\beta(\mathbf{x},\mathbf{x_0}),\omega\right) = 1. \tag{5}$$

The dipole may be described by a cosine (Sarradj, 2016, Eq. (10.30)) and thus the directivity reads

$$H_{\text{di}}\left(\beta(\mathbf{x},\mathbf{x_0}),\omega\right) = \cos\left(\beta(\mathbf{x},\mathbf{x_0})\right). \tag{6}$$

The formula of quadrupoles is given by Sarradj (2016, Eq. (10.41)) and depends on two directions. Hence, a longitudinal and a lateral quadrupole can be described

$$H_{\text{quad,long}}\left(\beta(\mathbf{x},\mathbf{x_0}),\omega\right) = \cos\left(\beta(\mathbf{x},\mathbf{x_0})\right)^2, \tag{7}$$

$$H_{\text{quad,lat}}\left(\beta(\mathbf{x},\mathbf{x_0}),\omega\right) = \cos\left(\beta(\mathbf{x},\mathbf{x_0})\right)\cos\left(\beta(\mathbf{x},\mathbf{x_0}) + \frac{\pi}{2}\right). \tag{8}$$

Note that Eq. (5) - (8) are reduced to the directivity pattern with unique amplitude.
A frequency dependent directivity pattern is the baffled circular piston model with radius Θ and a constant surface velocity. Its formula is given by (Skudrzyk, 1971, Eq. (26.42))

$$H_{\text{circ}}(\beta(\mathbf{x},\mathbf{x_0}),\omega) = \frac{2\,J_1\left(\frac{\omega}{c}\Theta\sin(\beta(\mathbf{x},\mathbf{x_0}))\right)}{\frac{\omega}{c}\Theta\sin(\beta(\mathbf{x},\mathbf{x_0}))}, \tag{9}$$

denoting the cylindrical Bessel function of first kind of first order as J_1 (Olver et al., 2010, Eq. (10.2.2)). Depending on the loudspeaker height Λ_y and the active radiating factor (ARF) α of the loudspeaker, the radius Θ of the circular piston may be calculated by (Schultz et al., 2015)

$$\Theta = \frac{\alpha\,\Lambda_y}{2}. \tag{10}$$

Note that the 3D circular piston has a circular symmetry around the main radiation axis, while the dipole and quadrupole directivity are plane mirrored on the x_1-x_2-plane. The circular piston model is widely used to model woofer and midrange speaker.

2.1.2 Free Space Green's Function

The three dimensional Green's function of point sources reads (Howe, 2002, Eq. (3.2.6))

$$G_{0,\mathrm{3D}}(\mathbf{x}, \mathbf{x_0}, w) = \frac{\mathrm{e}^{-\mathrm{j}\frac{\omega}{c}|\mathbf{x}-\mathbf{x_0}|}}{4\pi|\mathbf{x}-\mathbf{x_0}|} \tag{11}$$

and describes the sound propagation of an ideal point source from the source position $\mathbf{x_0}$ to the receiver position $\mathbf{x}$ at the angular frequency ω and is therefore called the acoustical transfer function (ATF). Further, air absorption is neglected in Eq. (11) and the speed of sound is given by (Möser, 2012, Eq. (2.18))

$$c = \sqrt{\frac{\gamma\, R\, T_0}{M_{\mathrm{mol}}}} = \sqrt{\frac{\gamma\, p_0}{\varrho_0}}. \tag{12}$$

For diatomic gases the isentropic exponent amounts to $\gamma \approx 1.4$, the density of air will be assumed with $\varrho \approx 1.2\,\mathrm{kg/m^3}$ and the atmospheric pressure is $101325\,\mathrm{Pa}$. Hence, the assumed speed of sound amounts to $c \approx 343\,\mathrm{m/s}$.

2.2 Adjoint-Based Monopole Synthesis

This section is based on Stein et al. (2019, Sec. 2). In Lemke (2015) the adjoint equations are derived and discussed in more detail, e.g., the adjoint Euler equations with initial and boundary conditions as well as the adjoint compressible Navier-Stokes equations.

In contrast to the commonly used frequency domain approaches for sound field generation (see Sec. 2.1), the adjoint-based method uses a representation of wave propagation in the time domain. Here, the full non-linear Euler equations are solved forward in time at the direct computation and the corresponding adjoint Euler equations are solved backward in time at the adjoint computation. Hereinafter, only the adjoint equations are described.

2.2.1 Adjoint Equations

The adjoint equations are introduced in a discrete version as in Giles and Pierce (2000). Moreover, the vector space is the full solution in space and time.
The adjoint equations arise by an objective function J, which is defined by the product between a geometric weight $\mathbf{g}$ and the system state $\mathbf{q}$

$$J = \mathbf{g}^\mathsf{T}\mathbf{q}, \qquad \mathbf{g}, \mathbf{q} \in \mathbb{R}^n, \tag{13}$$

where $\mathbf{q}$ corresponds to the solution of the governing system, which reads

$$A\mathbf{q} = \mathbf{s}, \qquad A \in \mathbb{R}^{n\times n}, \qquad \mathbf{s} \in \mathbb{R}^n. \tag{14}$$

Therein, A denotes the governing operator and $\mathbf{s}$ the sources. The computational effort of computing J can be reduced by the use of the adjoint equation

$$A^\mathsf{T}\mathbf{q}^* = \mathbf{g} \tag{15}$$

with $\mathbf{q}^*$ as the adjoint variable. Combining Eq. (13), Eq. (14) and Eq. (15) gives

$$J = \mathbf{q}^{*\mathsf{T}}\mathbf{s}. \tag{16}$$

After solving the adjoint equation, the objective J can be determined by a scalar product. Therefore gradients of the objective J can be computed efficiently.

2.2.2 Adjoint Sound Field Generation

The adjoint-based equations of Sec. 2.2.1 referred to sound field generation are given in this section. The total pressure p is given by

$$p = p_0 + p', \tag{17}$$

where the ambient pressure is $p_0 = 101325\,\text{Pa}$ and p' denotes the sound pressure. The adjoint-based equations arise by a so-called objective function

$$J = \frac{1}{2} \iint \left(p'(\mathbf{x},t) - p'_{\mathsf{ref}}(\mathbf{x},t)\right)^2 \sigma(\mathbf{x},t)\,\mathsf{d}\Omega, \tag{18}$$

where $p'(\mathbf{x},t)$ is now the sound pressure in the CAA model, $p'_{\mathsf{ref}}(\mathbf{x},t)$ is the reference target sound pressure provided by the CDPS model described in Sec. 2.1 and $\sigma(\mathbf{x},t)$ is an additional weight that defines the evaluation time and location of the objective function J defined in space and time with $\mathsf{d}\Omega = \mathsf{d}x_i\mathsf{d}t$. Optimal sound field generation is met, when J reaches a minimum regarding the sound pressure with subject to the Euler equations including the source forcing terms $\mathbf{s}(\mathbf{x},t)$:

$$\begin{aligned} \min_{p} \quad & J \\ \text{subject to} \quad & E(\mathbf{q}(\mathbf{x},t)) = \mathbf{s}(\mathbf{x},t). \end{aligned} \tag{19}$$

The constraint is the governing system abbreviating the Euler equations

$$\partial_t \begin{pmatrix} \varrho \\ \varrho u_j \\ \frac{p}{\gamma-1} \end{pmatrix} + \partial_{\mathbf{x}} \begin{pmatrix} \varrho u_i \\ \varrho u_i u_j + p\delta_{ij} \\ \frac{u_i p \gamma}{\gamma-1} \end{pmatrix} - u_i \partial_{\mathbf{x}} \begin{pmatrix} 0 \\ 0 \\ p \end{pmatrix} = \begin{pmatrix} 0 \\ 0 \\ s_p \end{pmatrix} \tag{20}$$

with the velocity $u(\mathbf{x},t)$, the density $\varrho(\mathbf{x},t)$ and γ as the heat capacity ratio. Optimizing the sound sources $\mathbf{s}(\mathbf{x},t)$ requires a linearization of Eq. (18) and the Euler equations in Eq. (19):

$$\delta J = \iint \underbrace{(p'(\mathbf{x},t) - p'_{\mathsf{ref}}(\mathbf{x},t))\sigma(\mathbf{x},t)}_{=g_p(\mathbf{x},t)} \delta p(\mathbf{x},t)\,\mathsf{d}\Omega \tag{21}$$

and

$$E_{\mathsf{lin}}(\mathbf{q_0}(\mathbf{x},t))\delta\mathbf{q}(\mathbf{x},t) = \delta\mathbf{s}(\mathbf{x},t) \tag{22}$$

with $\mathbf{g}(\mathbf{x},t) = [0,0,\Delta p(\mathbf{x},t)]^{\mathsf{T}}\sigma(\mathbf{x},t)$. The combination of Eq. (21) and Eq. (22) in Lagrangian manner with an (adjoint) multiplier $\mathbf{q}^*(\mathbf{x},t) = [\varrho^*(\mathbf{x},t), u_j^*(\mathbf{x},t), p^*(\mathbf{x},t)]^{\mathsf{T}}$ leads to

$$\begin{aligned}\delta J &= \iint \mathbf{g}^{\mathsf{T}}(\mathbf{x},t)\delta\mathbf{q}(\mathbf{x},t)\,\mathrm{d}\Omega - \iint \mathbf{q}^{*\mathsf{T}}(\mathbf{x},t)\underbrace{\left(E_{\mathsf{lin}}(\mathbf{q_0}(\mathbf{x},t))\delta\mathbf{q}(\mathbf{x},t) - \delta\mathbf{s}(\mathbf{x},t)\right)}_{=0}\mathrm{d}\Omega \\ &= \iint \mathbf{q}^{*\mathsf{T}}(\mathbf{x},t)\delta\mathbf{s}(\mathbf{x},t)\,\mathrm{d}\Omega + \iint \delta\mathbf{q}^{\mathsf{T}}(\mathbf{x},t)\left(\mathbf{g}(\mathbf{x},t) - E_{\mathsf{lin}}^{\mathsf{T}}(\mathbf{q_0}(\mathbf{x},t))\mathbf{q}^*(\mathbf{x},t)\right)\mathrm{d}\Omega.\end{aligned} \tag{23}$$

By demanding

$$\mathbf{g}(\mathbf{x},t) - E_{\mathsf{lin}}^{\mathsf{T}}(\mathbf{q_0}(\mathbf{x},t))\mathbf{q}^*(\mathbf{x},t) = 0, \tag{24}$$

the second term of the right hand side of Eq. (23) vanishes and the change of the objective function reads

$$\delta J = \iint \mathbf{q}^{*\mathsf{T}}(\mathbf{x},t)\delta\mathbf{s}\,\mathrm{d}\Omega. \tag{25}$$

The change of the objective function in Eq. (25) may be interpreted as a gradient of J with respect to the sources $\mathbf{s}(\mathbf{x},t)$:

$$\Delta_{\mathbf{s}} J = \mathbf{q}^*(\mathbf{x},t). \tag{26}$$

2.2.3 Monopole Sound Source

In contrast to the monopole implementation in frequency domain methods (e.g., Eq. (5)), the implementation in the present FDTD scheme is approximated by Gaussian distributions.

The equation of the Gaussian distribution reads

$$s_{\mathsf{g}}(\mathbf{x}) = 2\pi^{-\frac{3}{2}}(\sigma_{\mathsf{sd}}\Delta\mathbf{x})^{-3} \cdot \mathsf{e}^{-\frac{0.5}{(\sigma_{\mathsf{sd}}\Delta\mathbf{x})^2}(\mathbf{x}-\mathbf{x}_{\mathsf{s}})^2}, \tag{27}$$

where the standard deviation $\sigma_{\mathsf{sd}} = 2$ is used for all cases in this thesis. $\Delta\mathbf{x}$ is the increment of the discretized grid. Only cartesian grids are considered and $\Delta\mathbf{x}$ is chosen equally for all three spatial directions. The activation of the spatial expanded monopoles is attained by the multiplication with a forcing signal $s_{\mathsf{f}}(t)$ and thus defined in space and time:

$$s_p(\mathbf{x}, t) = s_{\mathsf{g}}(\mathbf{x}) \cdot s_{\mathsf{f}}(t). \tag{28}$$

Fig. 1 depicts a normalized 1D Gaussian distribution using Eq. (27) for two different grid discretization schemes. Small $\Delta\mathbf{x}$ cause less absolute spatial expansion of the distribution. One more way to reduce the spatial expansion might be the reduction of σ_{sd}. In that case the Gaussian distribution will have less supporting points (nodes) to generate the waves. Following Tam and Webb (1993) more than four nodes per wavelength are required to ensure a satisfactory CAA transmission behaviour. The disregard would directly reduce the CAA transmission behaviour and could cause parasitic, physically undesired waves. A corresponding analysis is omitted here.

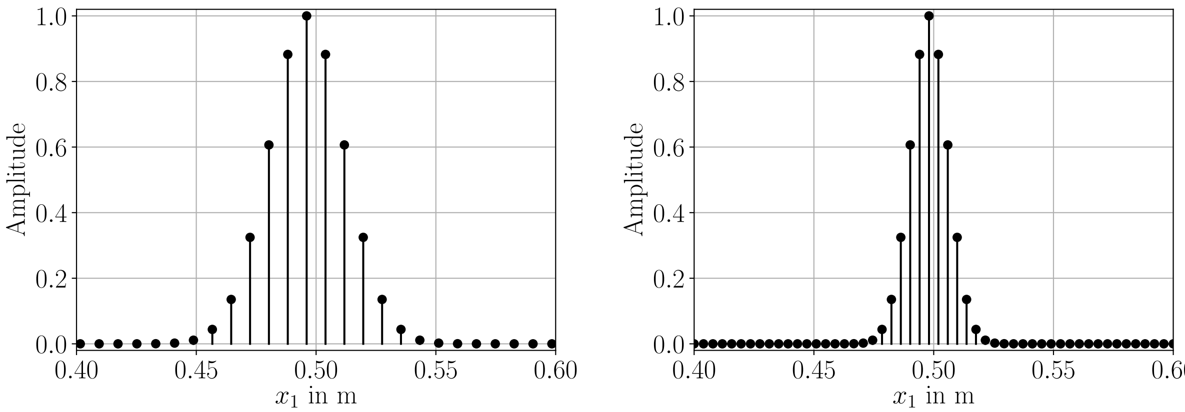

(a) $\Delta x \approx 7.87 \cdot 10^{-3}$ m, i.e., 128 grid points / m

(b) $\Delta x \approx 3.92 \cdot 10^{-3}$ m, i.e., 256 grid points / m

Fig. 1: Normalized Gaussian distribution on a 1D grid at $x_{\mathsf{s}} \approx 0.5$ m of two different grid discretization schemes.

2.2.4 Source Updating

To minimize the objective function J iteratively, the sound sources $s_p(\mathbf{x},t)$, which generate the sound field $p'(\mathbf{x},t)$, are adapted after the adjoint computation. The intended procedure to update the source distribution is separated into two steps.

At certain iteration loops n a monopole source is added to the existing source distribution. The source location of the added sound source $\mathbf{x}_\mathsf{s}$ is determined at the maximum time averaged gradient of J:

$$\mathbf{x}_\mathsf{s} = \mathbf{x}\left[\arg\max_{\mathbf{x}}\left(\left(\frac{1}{T}\sum_{t}^{T}(p^*(\mathbf{x},t))^2\right)\Psi(\mathbf{x})\right)\right]. \tag{29}$$

The variable $\Psi(\mathbf{x})$ is a mask function that spatially restricts the source region, e.g., the evaluation region of Eq. (29). $p^*(\mathbf{x},t)$ is the adjoint solution arised by the gradient of the objective function J with respect to the source forcing $s_\mathsf{f}(t)$. It provides the optimal position to minimize the objective (Lemke, 2015, Sec. 3.6.1). Thus, a minimization of the objective J may be reached in optimal sense by placing an additional monopole where $p^*(\mathbf{x},t)^2$ spatially maximizes. The source region is defined as a sphere around the directive point source $\mathbf{x_0}$ of the CDPS model. Thus, $\Psi(\mathbf{x})$ reads

$$\Psi(\mathbf{x}) = \begin{cases} 1 & \text{if} \quad |\mathbf{x}-\mathbf{x_0}| \leq r_\mathsf{s} \\ 0 & \text{else,} \end{cases} \tag{30}$$

where r_s denotes the source region radius.

Subsequently, the force term of the source distribution is updated at each iteration loop based on the gradient of the objective J, given in Eq. (26), by

$$s_\mathsf{f}^{[n+1]}(t) = s_\mathsf{f}^{[n]}(t) + \alpha_\mathsf{s}\Delta_s J, \tag{31}$$

where α_s denotes a step width and n the loop iteration number. The pressure term of the spatial expanded source $s_p^{[n+1]}$ is then constructed by Eq. (28). An appropriate choice of α_s is essential for the convergence behaviour of the steepest descent approach. Further information on the deployed line search technique can be found in Lemke (2015, Sec. 3.6.3).

2.2.5 Objective Area Mask Function

The objective area mask function $\sigma(\mathbf{x}, t)$ defines where and when the objective function (Eq. 18 and 21) is evaluated in space and time. The objective J is evaluated at every time step but spatially only within a predefined area. Therefore, $\sigma(\mathbf{x}, t)$ only varies on the spatial axes in this work:

$$\sigma(\mathbf{x}, t) = \frac{\operatorname{erf}\left[\frac{\sqrt{\pi}}{l}(\mathbf{r_0} - r_{\text{in}})\right] - \operatorname{erf}\left[\frac{\sqrt{\pi}}{l}(\mathbf{r_0} - r_{\text{out}})\right]}{2}, \qquad \mathbf{r_0} = |\mathbf{x} - \mathbf{x_0}|. \tag{32}$$

Therein, r_{in} denotes the effective start and r_{out} the effective end of the evaluation area, where $\sigma(\mathbf{x}, t) > 0.5$. l is a transition length of the mask edges and $\mathbf{r_0}$ contains the distance between all grid nodes and the acoustical center of the sound source defined in the CDPS model. The objective area mask function $\sigma(\mathbf{x}, t)$ is illustrated in Fig. 2 for $\mathbf{x_0} = 0.5$ m, $r_{\text{in}} = 0.2$ m, $r_{\text{out}} = 0.3$ m and $l = 0.05$ m on a 1D grid.

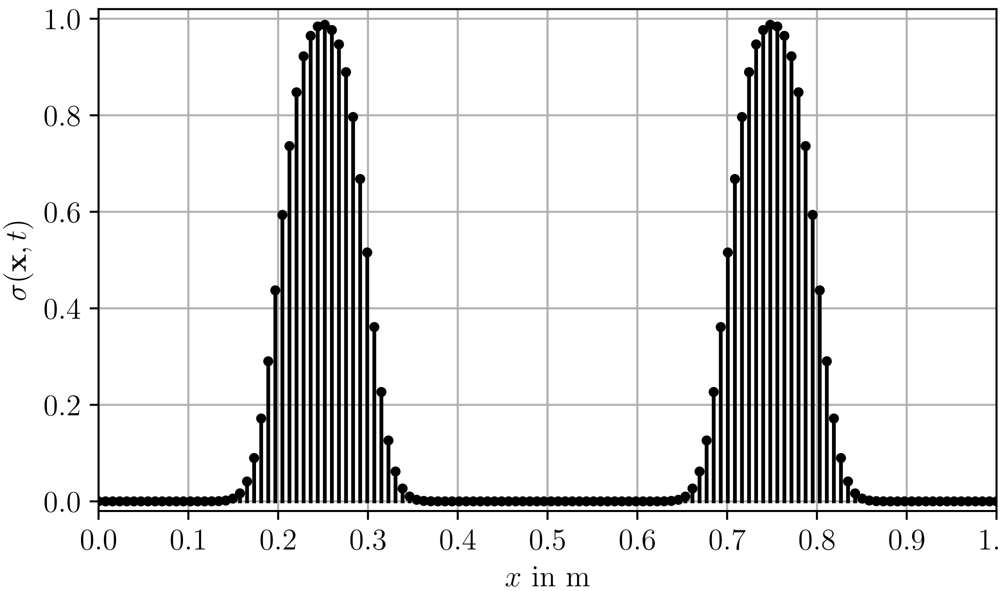

Fig. 2: 1D objective area mask function $\sigma(\mathbf{x}, t)$ with $\mathbf{x_0} = 0.5$ m, $r_{\text{in}} = 0.2$ m, $r_{\text{out}} = 0.3$ m and $l = 0.05$ m.

2.2.6 Iterative Process

A general overview of the iterative processing chain of the adjoint-based monopole synthesis method is depicted in Fig. 3.

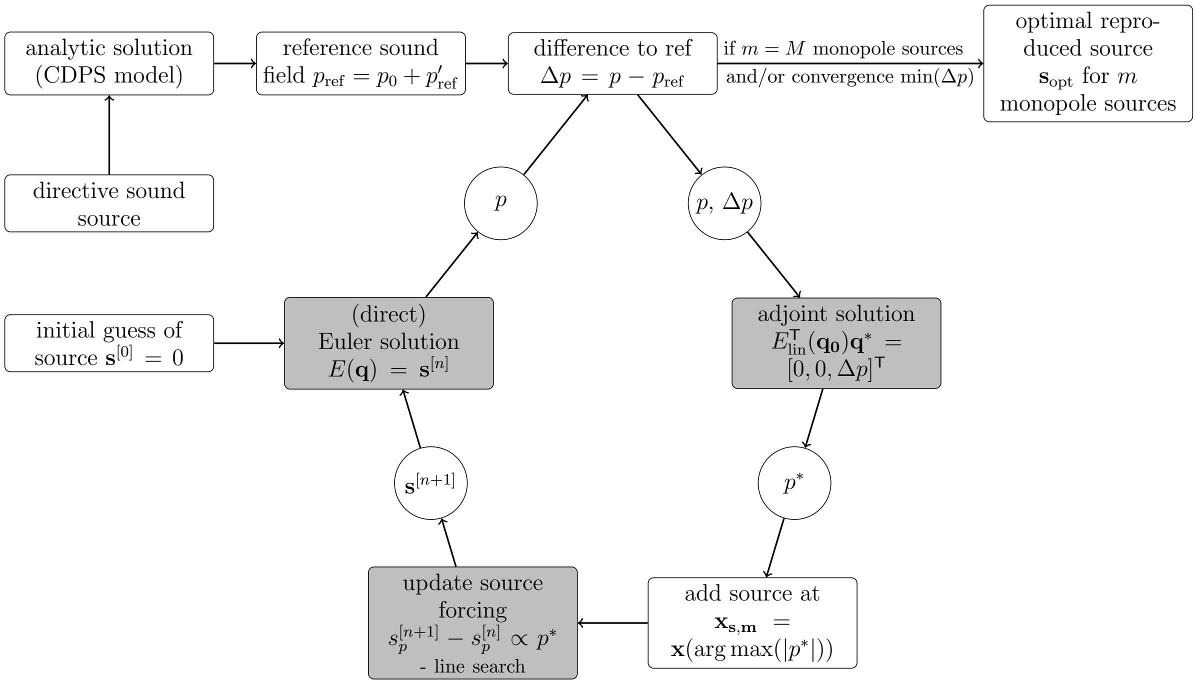

Fig. 3: Iterative process of the adjoint-based monopole synthesis method. Computationally intensive steps including CAA methods are marked in gray.

The process starts with an initial guess of the sound sources $s_p^{[0]} = 0$. The governing equations are solved forward in time. Subsequently, the results are compared with the reference state $p'_{\mathsf{ref}}(\mathbf{x}, t)$ provided by the CDPS model. The obtained difference $\Delta p(\mathbf{x}, t)$ drives the adjoint equations, which are solved backward in time. Further, the adjoint solution provides the gradient of $\Delta \mathbf{s}^{[n]} J$ to add a sound source and update the actual forcing of the sound sources $\mathbf{s}^{[n+1]}$. The process is repeated until the maximum amount of sound sources and convergence in terms of the objective function J is reached. If J increases during the iterative process, the loop iteration number n_{eval}

$$n_{\text{eval}} = \arg\min_{n}(J(n)) \tag{33}$$

is used and subsequently refined by a lower step width α_{s} until convergence is achieved. Note that in Eq. (33) J is defined over the loop iteration numbers n as each loop produces one value for J through Eq. (18). In the evaluation of the testcases in Sec. 5 only $n = n_{\text{eval}}$ is mentioned, but the refinement is always applied.

3 Simulation Settings and Setup

This section contains the settings of the CDPS solver and the CAA solver. An overview of the general settings is given in Tab. 1. Note that the case relevant CDPS settings are not listed in Tab. 1, but are described in the Secs. 5.2 - 5.5 of the testcases. Using the parameters of the grid, objective area, source region and the sponge area given in Tab. 1, a 2D slice of the x_1-x_2-plane ($x_3 = 0.5\,\mathrm{m}$) is depicted in Fig. 4. Claiming at least six grid points per wavelength, the cut-off frequency of $\Delta\mathbf{x}$ is $f_{\mathrm{c},\Delta\mathbf{x}} = c/(6 \cdot \Delta\mathbf{x}) \approx 7341\,\mathrm{Hz}$.

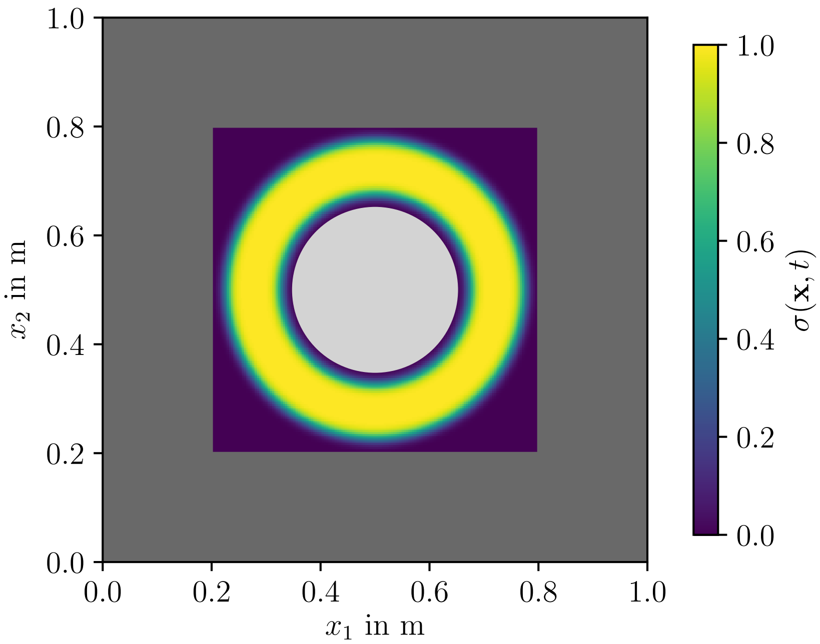

Fig. 4: 2D slice of the considered grid in the x_1-x_2-plane at $x_3 = 0.5\,\mathrm{m}$. The darkgrey painted area surrounding the boundaries represents the sponge area, the lightgrey circle area is the source region and the colorbar running from blue to yellow indicates the mask function values of the objective area $\sigma(\mathbf{x}, t)$.

CAA Solver

The CAA solver is discretized in a finite differences scheme in the time domain (FDTD). It means that the computation area is represented by a grid with a finite number of nodes. The underlying differential equation is replaced by an equivalent approximation (finite difference) at each node (Sesterhenn, 2018, p. 8). The necessary discretizations and settings to keep the error as low as possible are shortly described: the spatial discretization is applied with a sixth order accurate compact symmetric derivative stencil (Lele, 1992). The time discretization is employed by an explicit fourth-order Runge-Kutta scheme for time-wise integration (Sesterhenn, 2018, Sec. 5.4). All boundaries are handled as non-reflective using so-called "characteristic boundary conditions" (Poinsot and Lele, 1992; Stein, 2019). To further suppress reflections, a quadratic sponge layer is additionally added to all boundaries, acting on a side margin with a width of 0.2 m (Mani, 2012). The stability of the system is ensured with an implicit filter of sixth order applied at each time step (Gaitonde and Visbal, 2000). The CFL-number, which states the progression of a cell per time step (Courant et al., 1928), amounts to

$$\text{CFL} = \frac{u_{\text{tot}}\Delta t}{\Delta \mathbf{x}} = \frac{(\overbrace{|u|}^{=0} + c)\Delta t}{\Delta \mathbf{x}} = \frac{\sqrt{\frac{\gamma p_0}{\varrho_0}}\frac{1}{f_\text{s}}}{\Delta \mathbf{x}} \approx 0.908 \tag{34}$$

for the deployed constant node distance $\Delta \mathbf{x} \approx 7.87 \cdot 10^{-3}$ m. To ensure the stability of the method, the condition CFL < 1 should hold.

Tab. 1: Settings of the CDPS and CAA simulations.

variable / description	solver	value
$\mathbf{x}$	both	$0\,\mathrm{m} < x_i < 1\,\mathrm{m}$ for i=1,2,3
$\mathbf{x}_\mathrm{g}$	both	uniform, resolution $128 \times 128 \times 128$, except case (I)
$\Delta\mathbf{x}$	both	$\approx 7.87 \cdot 10^{-3}\,\mathrm{m}$, equidistant
f_s	both	48 kHz
ϱ_0	both	$\approx 1.21\,\mathrm{kg}/\mathrm{m}^3$
p_0	both	101325 Pa
γ	both	1.4
R_s	both	287
$D(\mathbf{x}, \omega)$	CDPS	1
$\mathbf{x_0}$	CDPS	$[0.5, 0.5, 0.5]^\mathrm{T}\,\mathrm{m}$, except case (II)
spatial discretization	CAA	sixth order accurate compact symmetric derivative stencil
CFL - number	CAA	≈ 0.908
time discretization	CAA	explicit fourth-order Runge-Kutta scheme
boundary condition	CAA	characteristic boundary condition: non-reflective
sponge	CAA	quadratic sponge with 0.2 m width
stability	CAA	implicit sixth order filter at each time step
objective area	CAA	$r_\mathrm{in} = 0.175\,\mathrm{m}$, $r_\mathrm{out} = 0.275\,\mathrm{m}$ and $l = 0.025\,\mathrm{m}$
source area	CAA	$r_\mathrm{s} = 0.15\,\mathrm{m}$

4 Evaluation Methods

The evaluation of the resulting sound fields $p'_{\text{ref}}(\mathbf{x},t)$ and $p'_{\text{opt}}(\mathbf{x},t)$ in Sec. 5.2 - 5.5 will be realized in the frequency domain. Thus, a discrete (fast) Fourier transform is applied

$$P_{\text{ref}}(\mathbf{x},\omega) = \mathcal{F}_t(p'_{\text{ref}}(\mathbf{x},t)) \qquad \text{and} \qquad P_{\text{opt}}(\mathbf{x},\omega) = \mathcal{F}_t(p'_{\text{opt}}(\mathbf{x},t)). \tag{35}$$

Subsequently, a normalization of each sound field is employed at $f = 2\,\text{kHz}$ and $\mathbf{x} = [0.8, 0.5, 0.5]^{\mathsf{T}}\,\text{m}$, which corresponds to $\varphi = 0\,\text{rad}$, $\vartheta = 0\,\text{rad}$ and $r = 0.3\,\text{m}$ in spherical coordinates with the origin at $\mathbf{x_0} = [0.5, 0.5, 0.5]^{\mathsf{T}}\,\text{m}$. This enables a comparison of $P_{\text{ref}}(\mathbf{x},\omega)$ and $P_{\text{opt}}(\mathbf{x},\omega)$ by various evaluation measures, which are described below.

Amplitude and Phase Spectrum

The amplitude and phase spectrum will be analyzed at three specific virtual microphone positions on the x_1-x_2-plane ($x_3 = 0.5\,\text{m}$). Fig. 4 is expanded by the microphone positions in Fig. 5 by red dots at $\mathbf{x}_{\text{mic},1} = [0.80, 0.50, 0.50]^{\mathsf{T}}\,\text{m}$, $\mathbf{x}_{\text{mic},2} = [0.76, 0.65, 0.50]^{\mathsf{T}}\,\text{m}$ and $\mathbf{x}_{\text{mic}\,3} = [0.21, 0.58, 0.50]^{\mathsf{T}}\,\text{m}$. The microphone positions expressed in polar coordinates on the x_1-x_2-plane ($x_3 = 0.5\,\text{m}$) amount for microphone 1: $r_{\text{mic}\,1} = 0.3\,\text{m}$, $\varphi_{\text{mic}\,1} = 0\,\text{rad}$, for microphone 2: $r_{\text{mic}\,2} = 0.3\,\text{m}$, $\varphi_{\text{mic}\,2} = \pi/6\,\text{rad}$ and for microphone 3: $r_{\text{mic}\,3} = 0.3\,\text{m}$, $\varphi_{\text{mic}\,3} = 11\pi/12\,\text{rad}$.

The amplitude spectrum $|P(\mathbf{x},\omega)|$ is the absolute value

$$|P(\mathbf{x},\omega)| = \sqrt{\Re\{P(\mathbf{x},\omega)\}^2 + \Im\{P(\mathbf{x},\omega)\}^2} \tag{36}$$

and the phase spectrum is the angle $\measuredangle P(\mathbf{x},\omega) = \phi(\mathbf{x},\omega)$

$$\measuredangle P(\mathbf{x},\omega) = \phi(\mathbf{x},\omega) = \arctan\left(\frac{\Im\{P(\mathbf{x},\omega)\}}{\Re\{P(\mathbf{x},\omega)\}}\right) \tag{37}$$

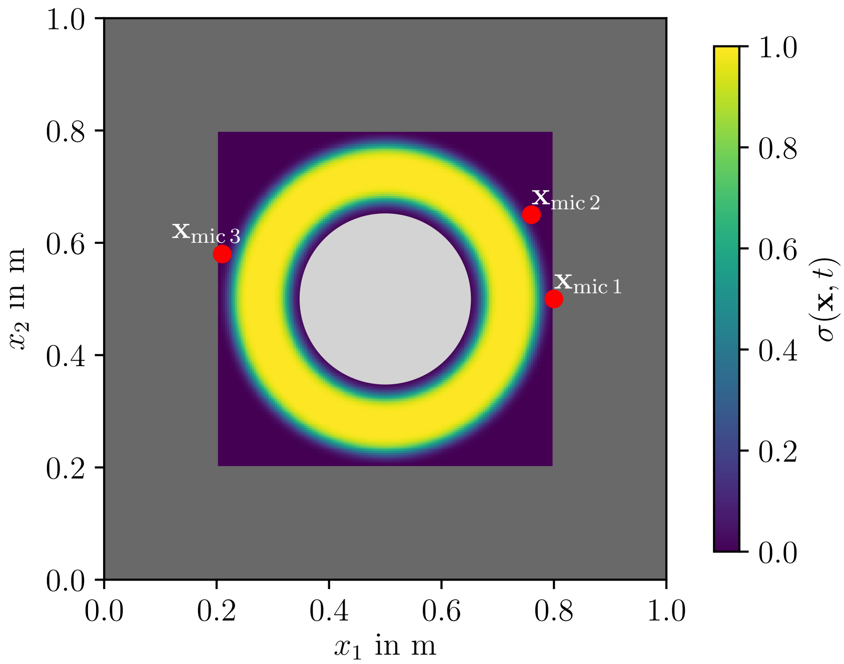

Fig. 5: Expanded view of Fig. 4: The virtual microphone positions are marked with red dots. For a further explanation see Fig. 4.

of the complex frequency spectrum $P(\mathbf{x}, \omega)$. The deviation of the reference and optimized sound fields will then be visualized. The amplitude figures are depicted as sound pressure level (SPL) deviation in $\mathsf{dB}_{\mathsf{rel}}$

$$\begin{aligned}(L_{p,\mathsf{opt}} - L_{p,\mathsf{ref}}) &= (20 \cdot \log_{10}(|P_{\mathsf{opt}}(\mathbf{x}, \omega)|) - 20 \cdot \log_{10}(|P_{\mathsf{ref}}(\mathbf{x}, \omega)|))\ \mathsf{dB}_{\mathsf{rel}} \\ &= 20 \cdot \log_{10}\left(\frac{|P_{\mathsf{opt}}(\mathbf{x}, \omega)|}{|P_{\mathsf{ref}}(\mathbf{x}, \omega)|}\right)\ \mathsf{dB}_{\mathsf{rel}} \end{aligned} \tag{38}$$

and finally smoothed by one neighbouring data point. The phase will also be shown as the deviation

$$(\phi_{\mathsf{opt}}(\mathbf{x}, \omega) - \phi_{\mathsf{ref}}(\mathbf{x}, \omega))\ \mathsf{rad}. \tag{39}$$

The phase deviation in percentage can be calculated by

$$\frac{\phi_{\mathsf{opt}}(\mathbf{x}, \omega) - \phi_{\mathsf{ref}}(\mathbf{x}, \omega)}{2\pi} \cdot 100\,\%. \tag{40}$$

Typically, the tolerance range of the phase deviation is smaller than $|10\,\%|$ or $|\pi/5|$ rad $\approx |0.628|$ rad.

2D Amplitude Directivity Pattern

The 2D directivity patterns are suitable to compare the reference and optimized sound source at a certain frequency f. Here, the x_1-x_2-plane ($x_3 = 0.5\,\mathrm{m}$) is considered. The directivity pattern is always determined at a circle radius of $r = 0.3\,\mathrm{m}$ around the reference sound source $\mathbf{x_0} = [0.5, 0.5, 0.5]^\mathsf{T}$ m. Thus, the circle radius is only applied at the azimuth angle φ. The 2D directivity patterns are logarithmically scaled

$$L_p(\mathbf{x}, \omega) = 20 \cdot \log_{10}\left(|P(\mathbf{x}, \omega)|\right)\ \mathrm{dB_{rel}} \tag{41}$$

and subsequently linearly smoothed by one neighbouring data point.

3D Amplitude Directivity Pattern

The 3D amplitude directivity figures, also known as balloon plots, may be used for a qualitative analysis. Thus, the circle radius $r = 0.3\,\mathrm{m}$ is applied for both spherical coordinates, the azimuth φ and the elevation ϑ. As the balloon plots shall suite for a qualitative analysis, no axis are employed in the figures and the absolute sound pressure with a subsequent linear smoothing of two neighbouring data points is shown.

FDTD Source Data

The determined source information of the CAA method are the forcing of the sources $s_{\mathrm{f},m}(t)$ and the source positions within the source region $\mathbf{x_{s,m}}$. Note that the forcing signals $s_{\mathrm{f},m}(t)$ will only be evaluated at the monopole center positions $\mathbf{x_{s,m}}$, where the normalized Gaussian distribution equals to one and thus

$$s_{p,m}(\mathbf{x},t) = s_{\mathsf{f},m}(t) \cdot \underbrace{s_{\mathsf{g},m}(\mathbf{x})}_{=1} = s_{\mathsf{f},m}(t) \qquad \text{for} \qquad \mathbf{x} = \mathbf{x_{s,m}}. \tag{42}$$

Considering both information may give a comprehension of the optimization process of the adjoint-based monopole synthesis method.

5 Testcases

5.1 Case (I): Implementation of the CDPS Solver

To speed up the workflow and to reduce the susceptibility to errors in the conversion between the CDPS solver in Matlab and the CAA solver written in the Fortran programming language, a CDPS solver is embedded into the architecture of the CAA solver. Hence, the CDPS solver could be easily parallelized by taking advantage of the existing Open MPI architecture (Gabriel et al., 2004) of the CAA solver. This enables an efficient computation of the reference sound fields.

Architecture

The CDPS module consists of a main routine called „sound field prediction" (`sfp`) that reads and allocates the parameters given in the `parameter.dat`-file. Subsequently, the main routine calls subroutines which are structured as follows:

1. Initialization of the frequency vector.
2. Computation of the driving functions. Note that the sources are uniformly driven in this thesis with $D(\mathbf{x_{0,m}}, \omega) = 1$, but included in the code as a segment for other possible applications.
3. `for-loop` over all sources $\mathbf{x_{0,m}}$:
    (a) Computation of the angle $\beta(\mathbf{x}, \mathbf{x_{0,m}})$ between the considered sound source and the receiver positions.
    (b) Computation of the directivity pattern given in Sec. 2.1.1.
    (c) Computation of the sound field transfer function $P(\mathbf{x}, \omega)$ and excitation of the sound field by the input signal $f_{\text{in}}(t)$ as described in Sec. 2.1.
4. Addition of all partial sound fields to $p'_{\text{out}}(\mathbf{x}, t)$.

5. Saving of the computed data in the `.h5`-format.

Comparison of the Implemetation in Matlab and Fortran

In this section the optimization of the computing time of the CDPS model in Fortran in contrast to the existing implementation in Matlab will be investigated. Moreover, the efficiency of the parallelization in Fortran is analyzed. The setup is as follows: One sound source with a circular piston directivity pattern is employed in a 3D grid of $32 \times 32 \times 32$ (A) and $64 \times 64 \times 64$ (B) grid nodes. The sound field is stimulated by a sine function of $f = 2\,\mathsf{kHz}$ with 1000 time steps. The sampling frequency $f_{\mathsf{s}} = 48\,\mathsf{kHz}$ is considered, which amounts to a physical time span of approximately $20.8\,\mathsf{ms}$. The simulation is then executed once with Matlab on one core and with Fortran parallelized on [1, 2, 4, 8, 16, 32, 64] cores.
The computing time of the considered cases is shown in Tab. 2. The CDPS solver in Fortran is approximately twice as fast as the Matlab solver (both executed on one core). Moreover, the execution time required by the Fortran program scales approximately linear with the used CPU cores. The computing time over the CPU parallelism cores is shown in a double logarithmic frame in Fig. 6. The deviations from the optimal linear scaling line are small. Besides, the visually larger deviation at 64 parallelism cores is tolerable due to the short computation time.
The Fortran CDPS solver makes use of an efficient implementation of the convolution with respect to time in the the time domain (see Eq. (4)), while the most efficient implementation in Matlab is to apply twice a Fourier transform and a multiplication:

$$p'(\mathbf{x},t) *_t f_{\mathsf{in}}(t) = \mathcal{F}_t^{-1}\left\{\mathcal{F}_t\left\{p'(\mathbf{x},t)\right\} \cdot \mathcal{F}_t\left\{f_{\mathsf{in}}(t)\right\}\right\}. \tag{43}$$

Note that even though the transfer function $P_{\mathsf{ATF}}(\mathbf{x},\omega)$ is computed in the frequency domain, it has to be transformed into the time domain due to the adapation to the test signal.
As outlined above, the computation time of the CDPS solver is eventually improved by the factor 2 for one CPU core. The parallelization linearly scales up to the considered 64 CPU cores.

Tab. 2: Computation time of the Matlab and Fortran implementation. Grid A consists of $32 \times 32 \times 32$ and Grid B of $64 \times 64 \times 64$ grid points (nodes).

Programming Language	Parallelism Cores	Time (Grid A)	Time (Grid B)
Matlab	1	44.82 s	438.05 s
Fortran	1	23.35 s	181.90 s
Fortran	2	11.26 s	94.88 s
Fortran	4	6.39 s	52.04 s
Fortran	8	3.21 s	25.49 s
Fortran	16	1.59 s	12.69 s
Fortran	32	0.80 s	6.39 s
Fortran	64	0.46 s	4.11 s

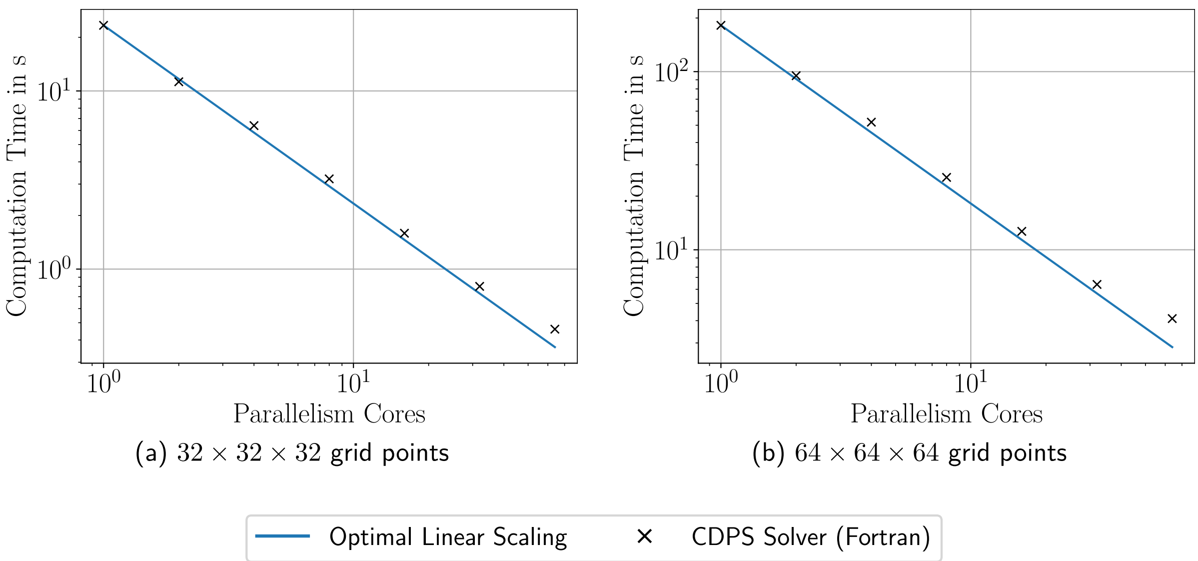

(a) $32 \times 32 \times 32$ grid points

(b) $64 \times 64 \times 64$ grid points

Fig. 6: Computation time over the parallelism cores of two grid discretization schemes.

5.2 Case (II): Nearest Distance of Neighbouring Monopoles

Sec. 2.2.3 describes that the considered monopole sound sources in the FDTD scheme are spatially expanded. If more than one monopole has to be implemented, as it is necessary in monopole synthesis approaches, it may lead to problematic interferences between sound sources if they are positioned too close to each other. This case shall ensure that the source positions $\mathbf{x}_{\mathrm{s}}$ do not interfere with each other in the following monopole synthesis cases in Sec. 5.3 - 5.5. It means that only the reproduction of the reference sound field is regarded, but not the directivity pattern itself.

Specific Settings and Setup

Two monopole sound sources are placed in a specific distance to each other. Step by step, the distance of the sources to each other is reduced until the centers of the monopole sound sources are at neighbouring grid nodes, i.e., one grid node distance to each other. The considered distances are listed in Tab. 3. The sources are stimulated with a band limited white noise (0.8 - 4.0 kHz) with 1000 time steps. Additionally, the test signals are in phase opposition to each other. Only one optimization loop is applied at each simulation of this case.

Results

The relative objective function J/J_{max} is depicted in Fig. 7 over the distance difference in grid points (nodes). It is here defined by a normalization over the cases with J_{max} as the maximum value of all cases. A minimum is present at 11 grid nodes distance. Polar figures of grid node distances between 7 and 25 nodes at 2 kHz are shown in Fig. 9. It can be seen that until 10 grid nodes in Fig. 9 (a-d) the deviation between $L_{p,\mathrm{ref}}$ and $L_{p,\mathrm{opt}}$ is below 1 dB, but increases with reduced grid node distance rapidly (see Fig. 9 (e-f)). Considering the 1D Gaussian distributions of the 11 grid nodes distance case in Fig. 8, an overlapping of the

Tab. 3: Considered monopole distances.

Δ grid nodes	$\mathbf{x}_{\text{dist}}$ in 10^{-3} m	Δ grid nodes	$\mathbf{x}_{\text{dist}}$ in 10^{-3} m
25	≈ 196.85	10	≈ 78.74
21	≈ 165.35	9	≈ 70.87
17	≈ 133.85	7	≈ 55.12
15	≈ 118.11	5	≈ 39.37
13	≈ 102.36	3	≈ 23.62
12	≈ 94.49	1	≈ 7.87
11	≈ 86.61		

Gaussian distributions is only observed at the edge of the Gaussian distribution where less than 10 % of the maximum amplitude is present.

Evaluation and Discussion

The increasing deviation between $p_{\text{ref}}(\mathbf{x}, t)$ and $p_{\text{opt}}(\mathbf{x}, t)$ for less than 10 grid nodes difference is comprehensible due to the increasing overlapping of the Gaussian distributions of the monopole sources. As the two input signals are in phase opposition, the cancellation of the Gaussian distributions to each other enlarges with decreasing $\mathbf{x}_{\text{dist}}$.
For more than 11 grid nodes distance, the reference directivity pattern shows more constrictions, but also a larger source expansion, which probably causes more near field shares in the directivity pattern. As a conclusion of the case, one may find that the distance between the centers of the monopole sources should be at least 11 grid nodes to ensure unfavorable influence to each other. Consequently, Eq. (30) is modified to

$$\Psi(\mathbf{x}) = \begin{cases} 1 & \text{if} \quad |\mathbf{x} - \mathbf{x_0}| \leq r_{\text{s}} \text{ and } |\mathbf{x} - \mathbf{x}_{\text{s,ex}}| \geq 11\Delta\mathbf{x} \\ 0 & \text{else,} \end{cases} \tag{44}$$

where $\mathbf{x}_{\mathrm{s,ex}}$ denotes the already existing monopole source center positions. Hence, Eq. (44) is implemented at the following cases in Sec. 5.3 - 5.5.

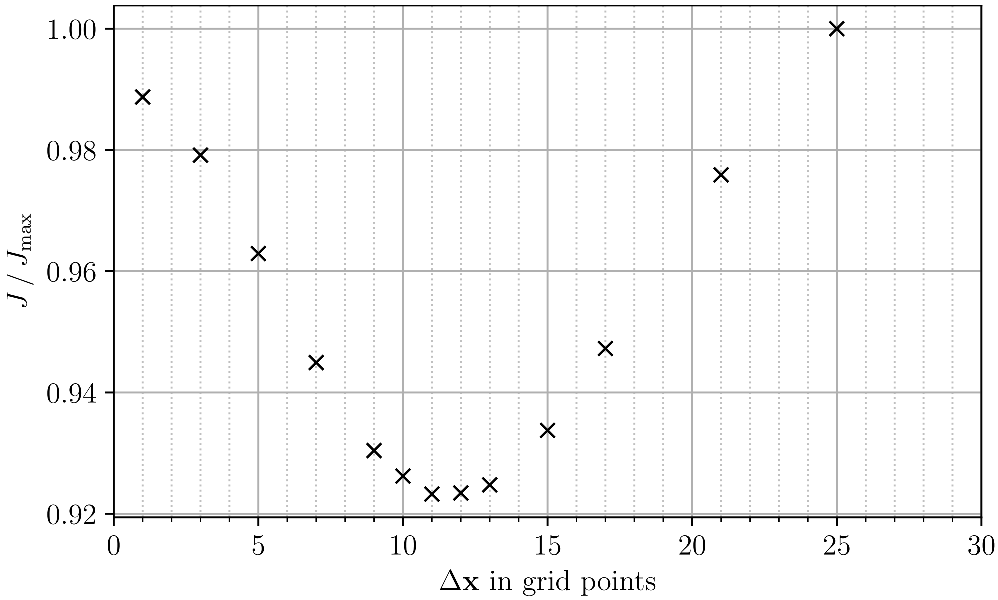

Fig. 7: Relative objective funtion $J\,/\,J_{\mathrm{max}}$ over distance between two monopole sources in grid points (nodes).

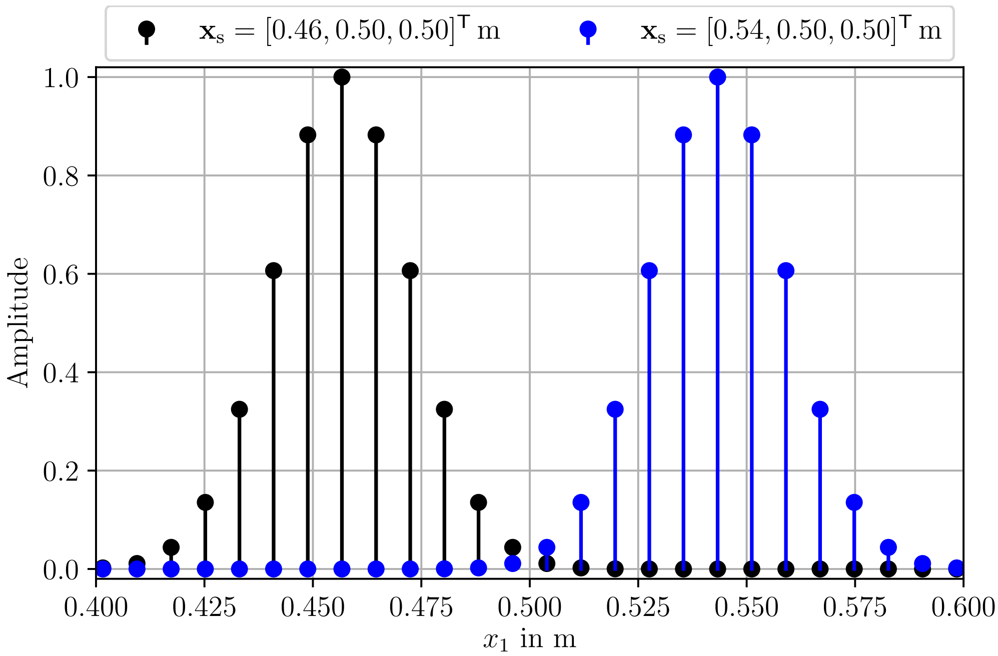

Fig. 8: Gaussian distribution of two monopoles with 11 grid nodes distance to each other.

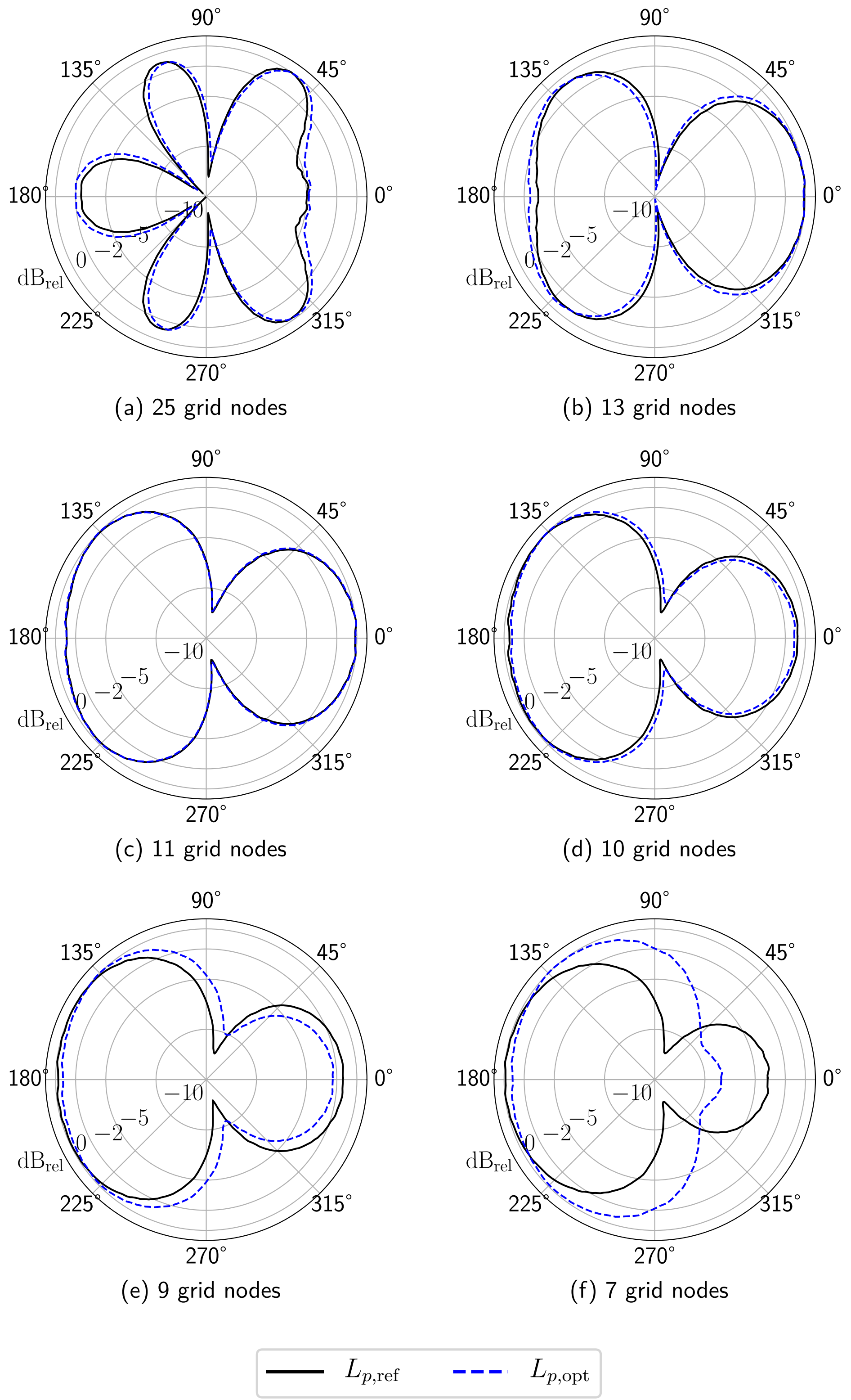

Fig. 9: Polar directivity patterns of two spatially distant monopoles with variable $\mathbf{x}_{\mathrm{dist}}$ at 2 kHz. The polar figures are taken on the x_1-x_2-plane ($x_3 = 0.5$ m) at the radius of 0.3 m from the center of the source at $[0.5, 0.5, 0.5]^{\mathsf{T}}$ m.

5.3 Case (III): Dipole

This case deals with the adjoint-based monopole synthesis method described in Sec. 2. The loop circle of the method (see Fig. 3) is repeated for $n = 30$ iteration loops while a monopole sound source is added every third loop.
The sound field is stimulated by a band limited white noise between 0.8 kHz and 4 kHz with 2000 time steps, which amounts to a physical time span of approximately 41.6 ms using the given parameters of Tab. 1. A similar case with slightly different settings was already presented in Lemke et al. (2020, Sec. „Klassische Monopolsynthese (A)“).

Evaluation and Discussion

The results are shown for the iteration loop $n = 20$ as it shows the lowest relative objective function value J_n/J_0 in Fig. 29 in App. A. Starting with the discussion of the forcing signals $s_{p,m}$, it can be seen in Fig. 10 that the forcing signals $s_{p,1}$ - $s_{p,3}$ are more than one order of magnitude larger than $s_{p,4}$ - $s_{p,7}$. An additional look at the relative objective function J_n/J_0 in Fig. 29 shows that the graph of the dipole is rapidly decreasing while adding the first three monopole sources. The following four monopole sources subsequently refine the dipole source. Further, the source forcing of $s_{p,2}$ and $s_{p,3}$ is approximately in phase opposition to $s_{p,1}$. Including the source positions in Fig. 11, the phase opposition enables a reinforcement in x_1-direction and a reduction in x_2- and x_3-direction. The source positions of $\mathbf{x_{s,4}}$ - $\mathbf{x_{s,7}}$ are located on the x_2-x_3-plane (x_1=0.5 m) and refine the reduction in both directions as their forcing signal is in phase opposition to the signals of $\mathbf{x_{s,2}}$ and $\mathbf{x_{s,3}}$.
Regarding the resulting sound fields, the deviation at the three virtual microphone positions in Fig. 12 is absolutely less than $2\,\mathrm{dB_{rel}}$ between 1.1 kHz and 2.9 kHz. In that range, the phase deviation is likewise low with a maximum of absolutely 0.2 rad. The 2D directivity patterns in Fig. 14 as well as the 3D directivity patterns in Fig. 13 confirm the behaviour that the dipole is well modeled in the range mentioned above. The discussion of the cut-off frequencies of the simulation settings used in the cases (III) to (V) can be found in Sec. 5.4. Comparing the visualization of the 2D directivity pattern at 1.5 kHz with Lemke et al. (2020,

Fig. 2), almost equal results are obtained. This supports the assumption from above that the monopole sources $\mathbf{x_{s,4}}$ - $\mathbf{x_{s,7}}$ only refine the dipole model, while the $\mathbf{x_{s,1}}$ - $\mathbf{x_{s,3}}$ mainly reproduce the dipole characteristic.

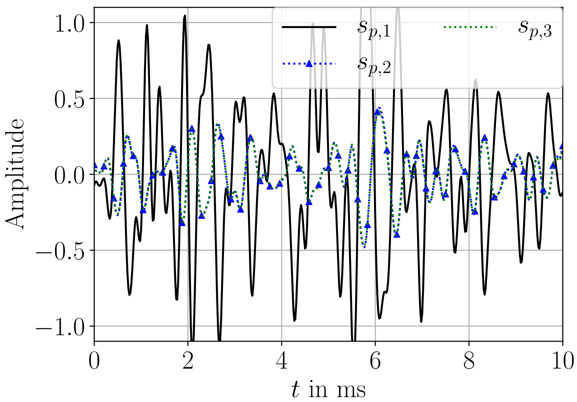

(a) force signals from $s_{p,1}$ to $s_{p,3}$

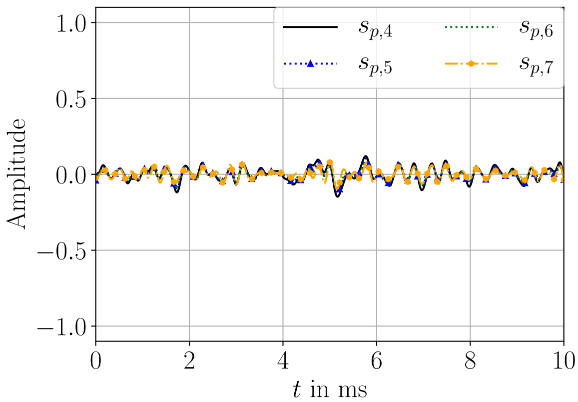

(b) force signals from $s_{p,4}$ to $s_{p,7}$

Fig. 10: Extract between $t = 0$ ms and $t = 10$ ms of the force signals $s_{p,m}$ of the determined monopole sources $\mathbf{x_{s,m}}$ of the dipole.

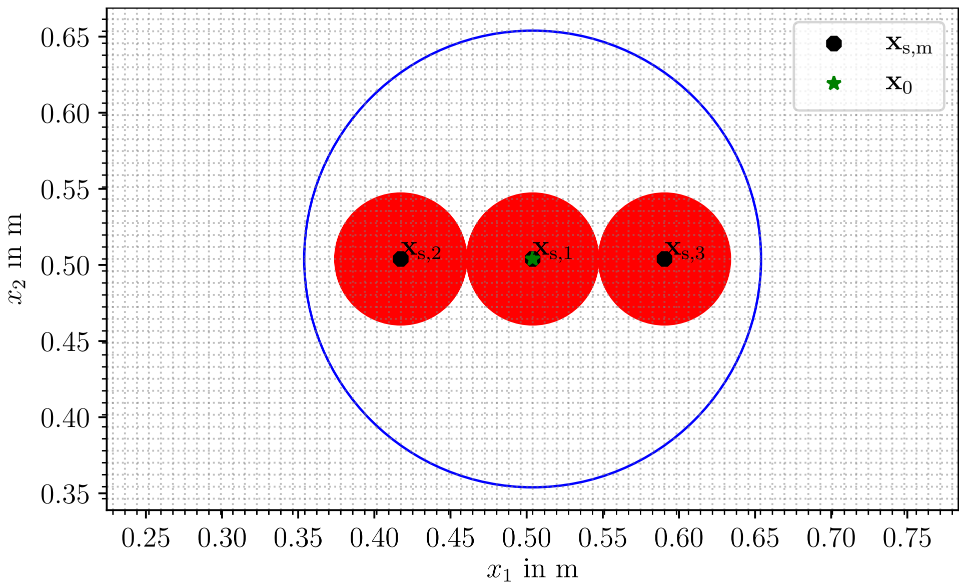

Fig. 11: Determined source positions of $\mathbf{x_{s,1}}$ - $\mathbf{x_{s,3}}$ on the x_1-x_2-plane ($x_3 = 0.5$ m) are marked by an octagon. The green star marks the position of the reference sound source $\mathbf{x_0}$. The red painted circles mark the spatial expansion of the monopole sources and the blue circle is the source region with an radius of $r_s = 0.15$ m. The coordinate grid corresponds to the spatial discretization.

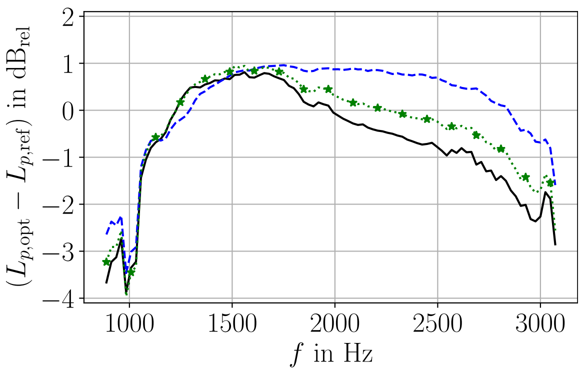

(a) SPL deviation

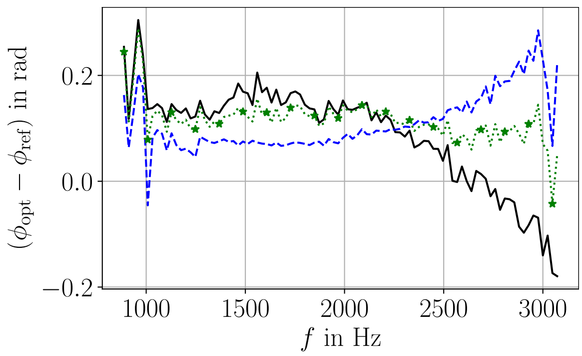

(b) Phase deviation

Fig. 12: SPL and Phase deviation of the reference and optimized sound field at the virtual microphone positions. Microphone 1 is at $[0.8, 0.5, 0.5]^\mathsf{T}$ m, microphone 2 at $[0.76, 0.65, 0.50]^\mathsf{T}$ m and microphone 3 at $[0.21, 0.58, 0.50]^\mathsf{T}$ m.

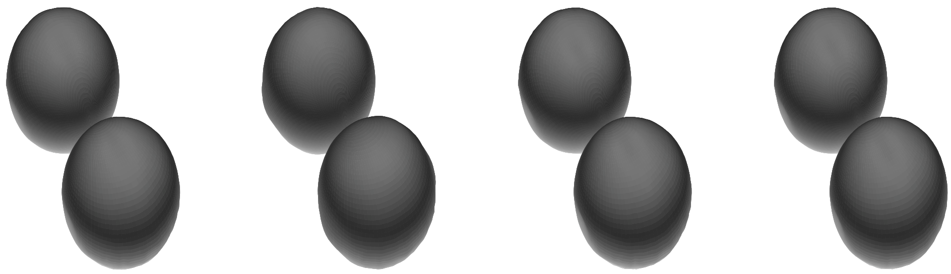

(a) 1.5 kHz (b) 2.0 kHz (c) 2.5 kHz (d) 3.0 kHz

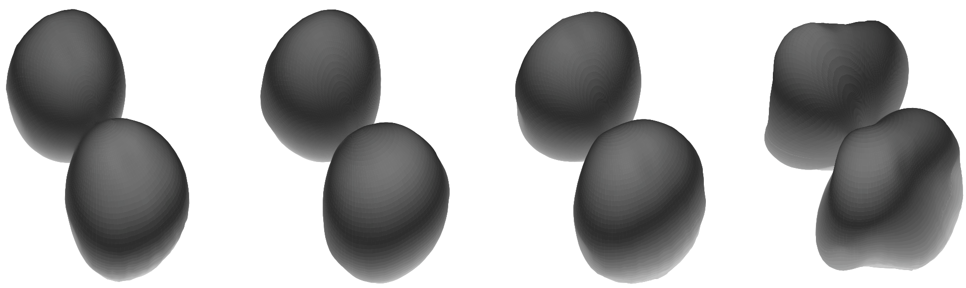

(e) 1.5 kHz (f) 2.0 kHz (g) 2.5 kHz (h) 3.0 kHz

Fig. 13: Amplitude balloon plots of the reference (a-d) and optimized (e-h) dipole source. The plots are taken at the circle radius $r = 0.3\,\mathrm{m}$ from the center of the source at $[0.5, 0.5, 0.5]^\mathsf{T}$ m.

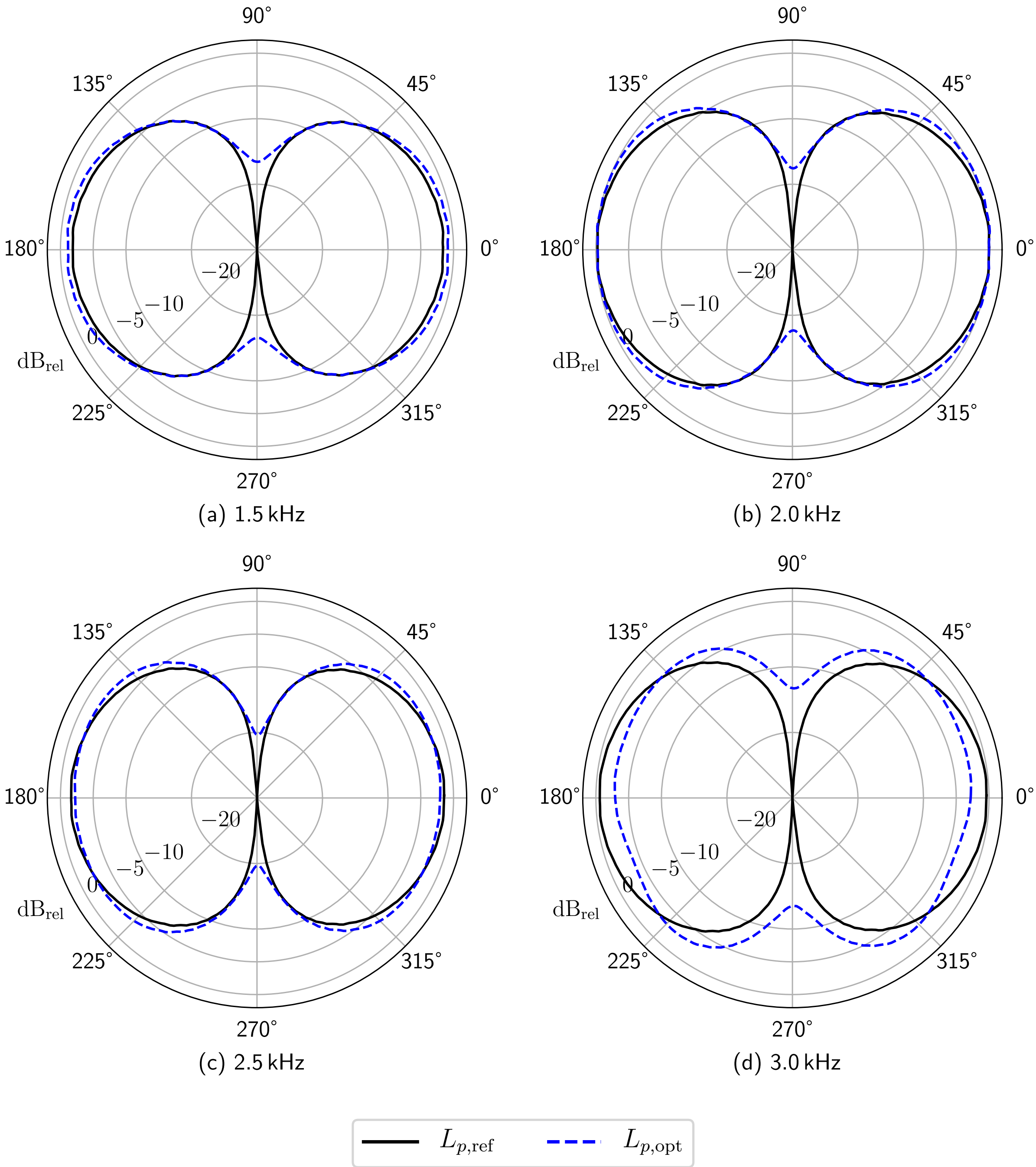

Fig. 14: Polar directivity patterns of the reference and optimized dipole source. The figures are taken at the circle radius $r = 0.3$ m from the center of the source at $[0.5, 0.5, 0.5]^{\mathsf{T}}$ m on the x_1-x_2-plane ($x_3 = 0.5$ m).

5.4 Case (IV): Quadrupole

The modeling of a lateral quadrupole sound source is pursued in this case, which is given in Eq. (8). It is applied as a frequency and phase constant model, but more complex in comparation to the dipole in Sec. 5.3, caused by the multiple constrictions of the quadrupole. The input signal is equal to Sec. 5.3 (white noise, 0.8 - 4.0 kHz, 2000 time steps).

Evaluation and Discussion

The loop iteration number $n = 27$ is evaluated because it provides the lowest relative objective value J_n/J_0 (see Fig. 29). The results of the evaluation methods described in Sec. 4 are depicted in Fig. 15 - 19.

Analyzing the source positions and their forcing in Fig. 15 and Fig. 16, a recurring algorithm of placing and forcing the source terms can be determined. The first monopole source is placed by the monopole synthesis method at the same position as the reference directive source and has the strongest forcing signal. The four following added monopole sources surround the first monopole source by

$$\varphi = i \cdot \frac{\pi}{2} + \frac{\pi}{4} \qquad \text{with} \qquad i = 0, 1, 2, 3 \tag{45}$$

and $r \approx 0.089\,\mathrm{m}$ which corresponds to approximately 11 grid nodes. Their forcing signals are nearly identical (see Fig. 15 (a)) and are approximately in phase opposition to $s_{p,1}$ (similar to Sec. 5.3). The same behaviour may be observed for the next four monopole sources too, where $\varphi = i \cdot (\pi/2)$ with $i = 0, 1, 2, 3$ and a wider radius of 16 grid nodes is present (except $\mathbf{x_{s,6}}$ with 18 grid nodes).

Thus, it is concluded that the adjoint optimization process of a quadrupole can be reduced by only locating the first source of each source circle around $\mathbf{x_{s,1}}$ or $\mathbf{x_0}$. The positions of the following three monopole sources can be calculated by Eq. (45) and the nearest possible radius to the first monopole source at the acoustic center. Hence, the amount of possible source circles depends on the grid discretization and the given source region radius r_s. Analyzing

Fig. 29 in the App. A, the relatively steepest decrease is at $n = 1, 13, 25$, that corresponds to the loop iteration number n when a circle is "completely filled" by monopole sources. Thus, the number of deployed monopole sources should be

$$m = 1 + 4i, \quad i \geq 0 \in \mathbb{Z}. \tag{46}$$

Considering the resulting sound fields, it can be noticed in Fig. 17 (a) that the SPL deviation of microphone 1 between 1.7 kHz and 2.7 kHz is below $1\,\mathrm{dB_{rel}}$, but increases outside that range. A possible explanation of the large deviation at the low-frequency edge of 1 kHz is the corresponding wavelength of 0.343 m. This wavelength has the same order of magnitude as the computational domain and such might suffer from cut-off effects and a less functional sponge boundary (Stein et al., 2020). An explanation of the deviation above 2.5 kHz might be the disregard of the far-field condition suggested by Möser (2012, p. 109)

$$\frac{r}{l_\mathrm{s}} > \frac{l_\mathrm{s}}{\lambda}, \tag{47}$$

where l_s is the expansion of the sound source. Assuming $l_\mathrm{s} = 0.2\,\mathrm{m}$, the cut-off frequency is $f_\mathrm{c} \approx 2570\,\mathrm{Hz}$. The large deviation of microphone 2 accounts to the strong constriction of the quadrupole source at 30 deg with approximately $-12\,\mathrm{dB}$ and is only in a small range between 2.3 kHz and 2.7 kHz below $1\,\mathrm{dB_{rel}}$. At 2.0 kHz the deviation is $2.0\,\mathrm{dB_{rel}}$, but the qualitative reproduction in Fig. 19 (b) is satisfactory at 30 deg. Thus, larger deviations at the constrictions of the directivity pattern are tolerable, e.g., if the reference states $-\infty\,\mathrm{dB}$, a reproduction with $-15\,\mathrm{dB}$ is adequate (see Fig. 19 (b)). The phase deviation in Fig. 17 (b) is relatively low with a maximum of $\pm 0.2\,\mathrm{rad}$ (exluding the collapse at 1 kHz) or expressed in percentage $(0.2/2\pi) \cdot 100\,\% \approx 3.2\,\%$.

The 2D directivity patterns in Fig. 19 confirm the observations of Fig. 17, that the reproduction of the directivy pattern at 2.0 kHz and 2.5 kHz is satisfactory, while larger deviation may be observed at 1.5 kHz and 3.0 kHz. This behaviour is further qualitatively confirmed by the 3D directivity patterns in Fig. 18.

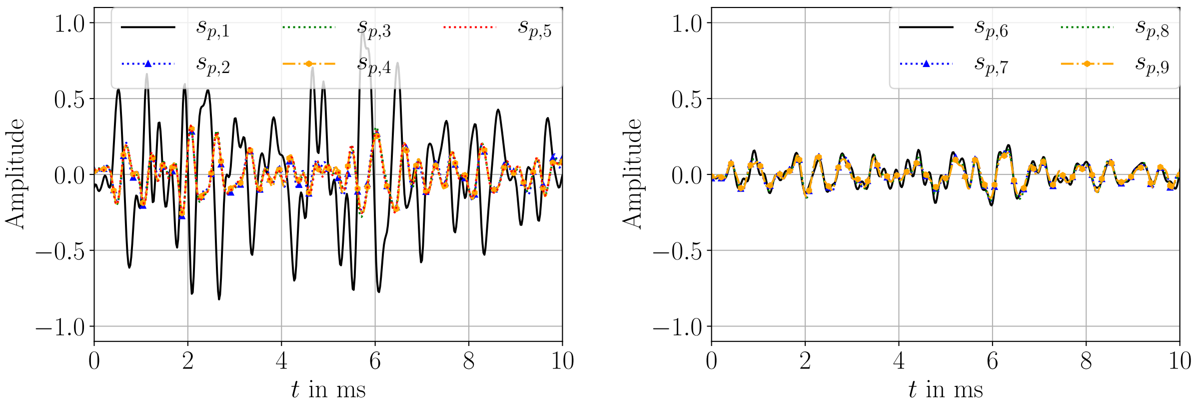

(a) force signals from $s_{p,1}$ to $s_{p,5}$

(b) force signals from $s_{p,6}$ to $s_{p,9}$

Fig. 15: Extract between $t = 0\,\mathrm{ms}$ and $t = 10\,\mathrm{ms}$ of the force signals $s_{p,m}$ of the determined monopole sources $\mathbf{x_{s,m}}$.

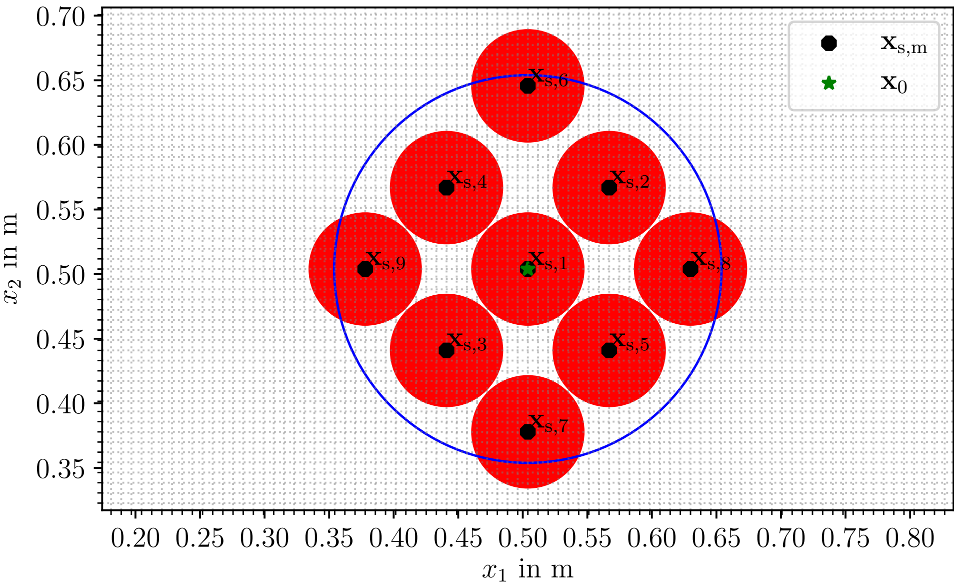

Fig. 16: Determined source positions of loop iteration number $n = 27$ in the x_1-x_2-plane ($x_3 = 0.5\,\mathrm{m}$) are marked by an octagon. The green star markes the position of the reference sound source $\mathbf{x_0}$. The red painted circles mark the spatial expansion of the monopoles and the blue circle is the source region with an radius of $r_\mathrm{s} = 0.15\,\mathrm{m}$. The coordinate grid corresponds to the spatial discretization.

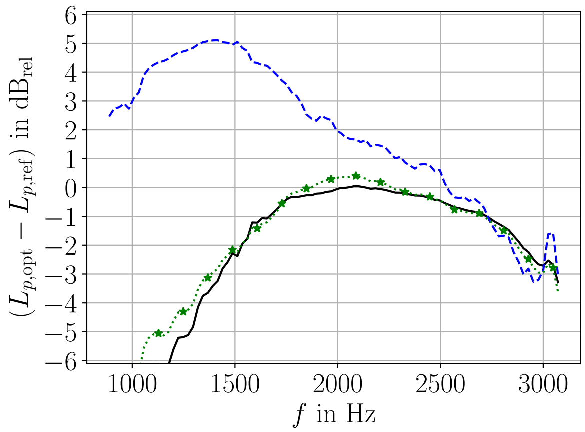

(a) SPL deviation

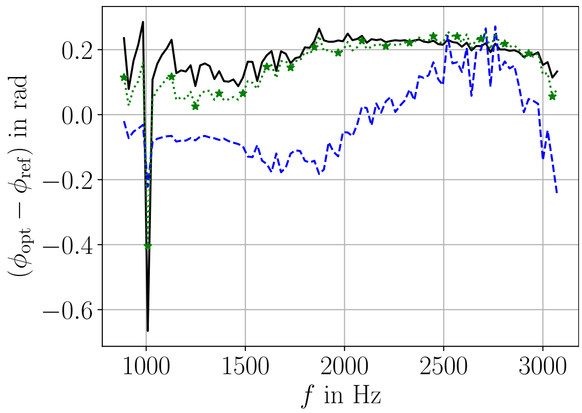

(b) Phase deviation

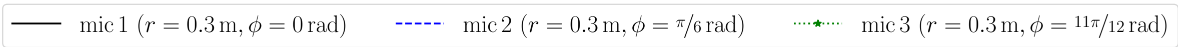

Fig. 17: SPL and phase deviation of the reference and optimized sound field. Microphone 1 is at $[0.8, 0.5, 0.5]^\mathsf{T}$ m, microphone 2 at $[0.76, 0.65, 0.50]^\mathsf{T}$ m and microphone 3 at $[0.21, 0.58, 0.50]^\mathsf{T}$ m.

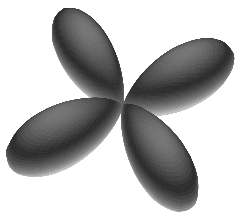
(a) 1.5 kHz

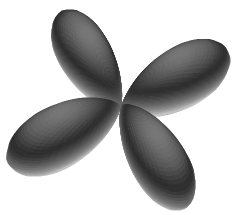
(b) 2.0 kHz

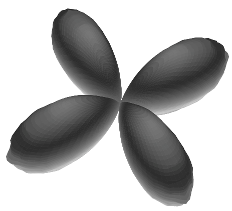
(c) 2.5 kHz

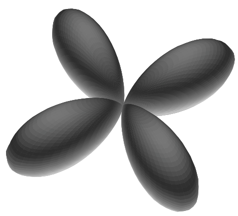
(d) 3.0 kHz

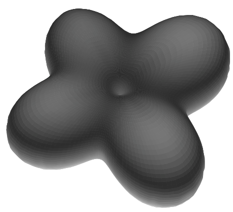
(e) 1.5 kHz

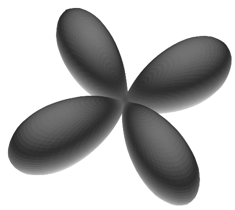
(f) 2.0 kHz

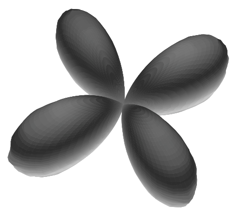
(g) 2.5 kHz

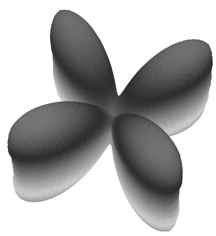
(h) 3.0 kHz

Fig. 18: Amplitude balloon plots of the reference (a-d) and optimized (e-h) quadrupole. The plots are taken at the circle radius $r = 0.3\,\mathrm{m}$ from the center of the source at $[0.5, 0.5, 0.5]^\mathsf{T}$ m.

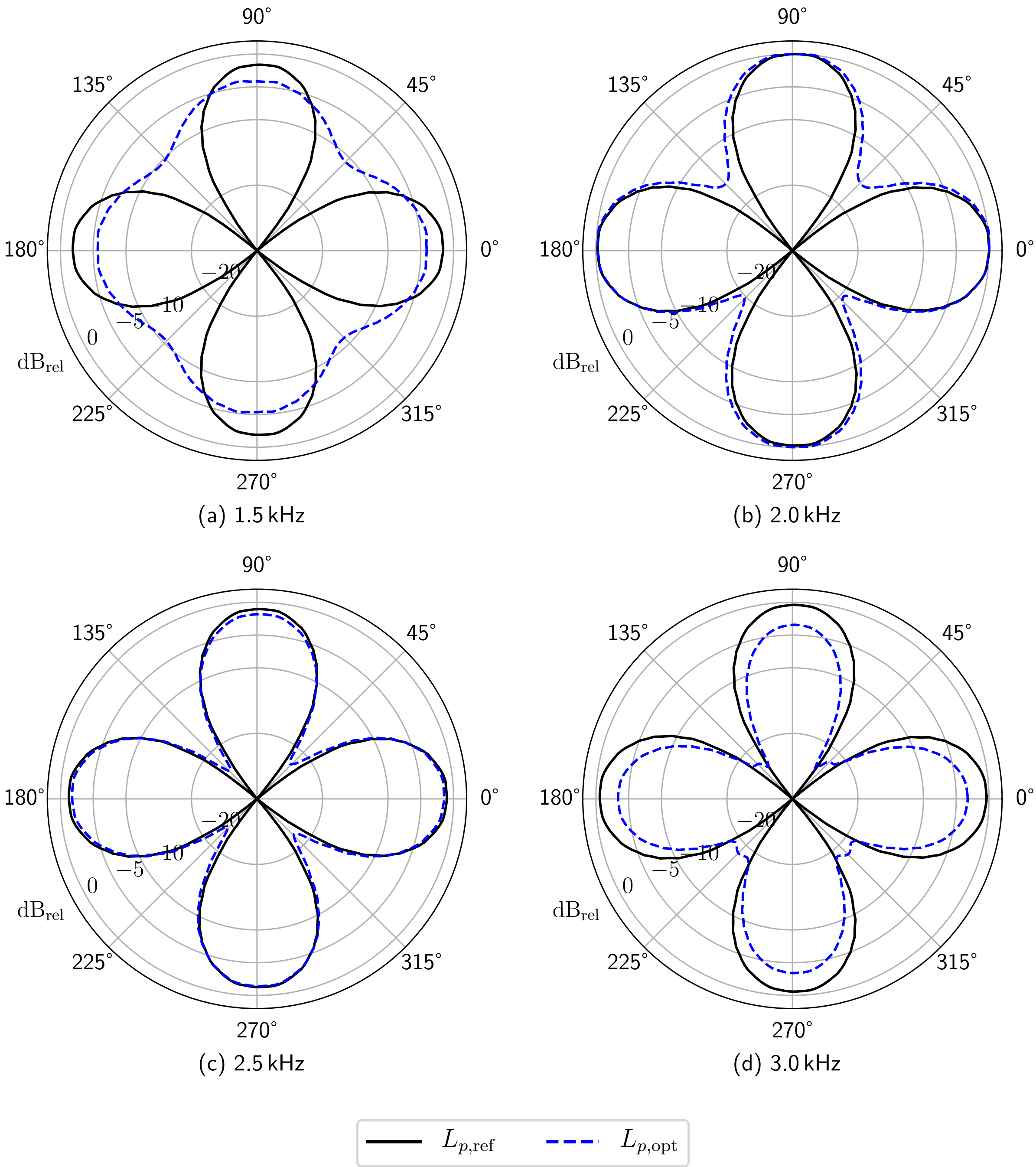

Fig. 19: Polar directivity patterns of the reference and optimized quadrupole. The figures are taken at the circle radius $r = 0.3$ m from the center of the source at $[0.5, 0.5, 0.5]^{\mathsf{T}}$ m on the x_1-x_2-plane ($x_3 = 0.5$ m).

5.5 Case (V): (Complex) Circular Piston

The circular piston model is widely used to model an idealized 2-way woofer and midrange speaker. Its formula is given in Eq. (9), where the amplitude of the model is frequency dependent, but the phase is constant. Usually, realistic, measured loudspeaker directivity patterns are measured as impulse responses in the time domain and subsequently Fourier transformed into a complex transfer function in the frequency domain. Therefore, Eq. (9) is subsequently expanded by a frequency and a location dependent complex exponential function:

$$H_{\mathsf{ccp}}(\beta(\mathbf{x}, \mathbf{x_0}), \omega) = \frac{2\, J_1\left(\frac{\omega}{c}\Theta \sin(\beta(\mathbf{x}, \mathbf{x_0}))\right)}{\frac{\omega}{c}\Theta \sin(\beta(\mathbf{x}, \mathbf{x_0}))} \cdot \mathsf{e}^{\mathsf{j}\frac{\omega}{c}K} \cdot \mathsf{e}^{\mathsf{j}\beta(\mathbf{x}, \mathbf{x_0})K}, \tag{48}$$

where K is a scaling parameter. The chosen loudspeaker parameters are the loudspeaker height $\Lambda_y = 0.2\,\mathrm{m}$ and the active radiating factor $\alpha = 0.82$. According to Eq. (10), the radius of the circular piston amounts to $\Theta = 0.082\,\mathrm{m}$. The complex exponential functions result in a phase rotation in terms of the variable frequency and the radiation angle, since a complex exponential function can be expressed by Euler's formula

$$\mathsf{e}^{\mathsf{j}\beta} = \cos(\beta) + \mathsf{j}\sin(\beta). \tag{49}$$

The real circular piston (Case Va) given in Eq. (9) may be described by Eq. (48) with $K = 0.0$ as well. Subsequently, a complex circular piston will be analyzed for $K = 0.1$ (Case Vb) and for a faster phase rotation by $K = 1.0$ (Case Vc).
Again, similar to Sec. 5.3, the test signal is a band-limited white noise (0.8 - 4.0 kHz, 2000 time steps).

Evaluation and Discussion

Fig. 29 shows that the minimum of the relative objective function is present at the loop iteration number $n = 23$ for the real and the complex circular piston and is therefore evaluated.

First, considering the forcing signals of the real circular piston in Fig. 20 together with the source positions $\mathbf{x_{s,m}}$ in Tab. 4, a similar behaviour to the previous sections is observed: $s_{p,1}$ is the „main" monopole source, while $s_{p,2}$ and $s_{p,3}$ have a reduced and anti-phased signal to $s_{p,1}$. Further, $\mathbf{x_{s,1}}$ is surrounded by $\mathbf{x_{s,2}}$ and $\mathbf{x_{s,3}}$. $\mathbf{x_{s,4}}$ - $\mathbf{x_{s,8}}$ are positioned on the x_2-x_3-plane ($x_1 = 0.5$ m) and refine the source modeling. As the circular piston is a frequency dependent model, a closer look at the amplitude frequency spectrum of the forcing signals $s_{p,1}$, $s_{p,2}$ and $s_{p,4}$ might be of interest and is depicted as the deviation of $s_{p,2}$ and $s_{p,4}$ to $s_{p,1}$ in Fig. 21. It demonstrates that almost only $s_{p,1}$ is activated at low frequencies around 1 kHz. Here, the directivity pattern of the circular piston has a monopole-like character. With increasing frequency the other monopole sources are continuously activated and show only approximately 3 dB difference to $s_{p,1}$ at 3 kHz where the first side lobes begin to spread. To clarify the evolution process, Fig. 25 depicts the 3D directivity patterns for $n = [3, 6, 9, 12, 15, 18, 21, 23]$ at $f = 2.5$ kHz. As described, the first three monopoles at $n = 9$ (Fig. 25 (c)) already shape the dipole character of the model at $f = 2.5$ kHz. Following the directivity pattern is refined until $n = 23$.

Analyzing the reproduction of the reference directivity pattern at the virtual microphone positions, Fig. 22 shows that they are correctly captured about the whole analyzed frequency range with a maximum deviation of ± 2 dB. The polar plots in Fig. 23 confirm this behaviour, but show deviations at the side lobe at $\pi/2$ rad and $3\pi/2$ rad at $f = 3$ kHz. The adjoint-based optimization gives less prominence to regions with small SPL values and can therefore not capture the small side lobes correctly, if a low amount of monopoles is used. In this context, it can be assumed that more monpoles are necessary. It is considered in the work of Stein et al. (2020, Fig. 8) that includes—as mentioned in Sec. 1.2—a grid- and adjoint-based monopole synthesis method. It means, that all grid nodes in a specific source regions are assumed as monopole source, i.e., Dirac functions, with the condition that the Euler equations hold. Comparing the results with the findings of Stein et al. (2020, Fig. 8), the observed deviations of the polar plots are throughout larger. Due to the variable location and the higher number of monopoles, the grid-based method is superior to the considered method in this thesis, that uses spatially expanded monopoles. Besides a higher spatial discretization was applied in the work of Stein et al. (2020).

Analyzing the complex circular piston model given in Eq. (48) for $K = 0.1$, the amplitude and phase spectra are shown in Fig. 26. The deviation is almost equal to the results of the completely real circular piston case ($K = 0.0$). The 3D directivity patterns of the complex circular piston in Fig. 27 show almost the same shapes as Fig. 24. Different to $K = 0.1$, the amplitude and phase spectra of the complex circular piston with $K = 1.0$ in Fig. 28 shows deviations up to approximately $4.3\,\mathrm{dB_{rel}}$ and $1.4\,\mathrm{rad}$. Thus, it can be concluded that the method is able to reproduce complex directivity pattern for slow phase variations in the same manner as completely real directivity pattern. However, fast phase variations obviously require more monopoles similar to the findings with respect to the amplitude variations. In summary, the more and stronger the variations in terms of phase and amplitude are, the more monopoles are necessary for satisfactory reproduction of the directive sound source.

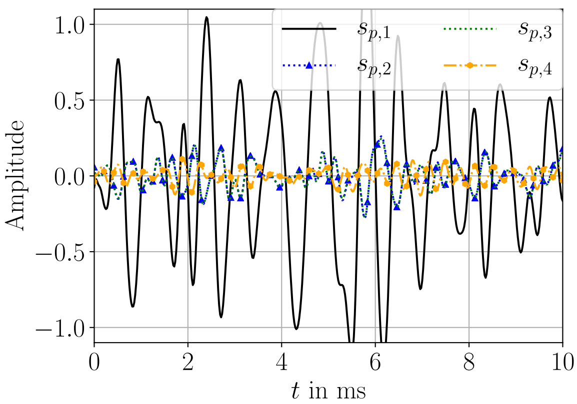

(a) force signals from $s_{p,1}$ to $s_{p,4}$

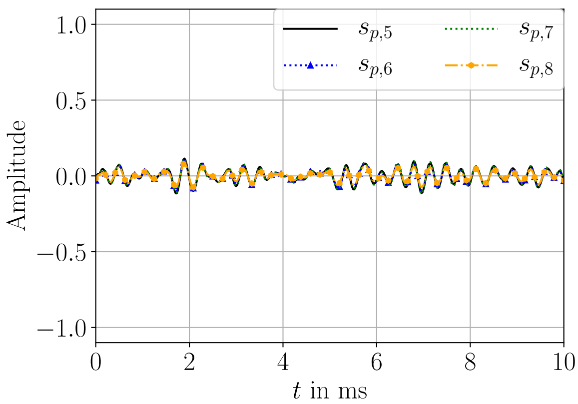

(b) force signal from $s_{p,5}$ to $s_{p,8}$

Fig. 20: Extract between $t = 0\,\mathrm{ms}$ and $t = 10\,\mathrm{ms}$ of the force signals $s_{p,m}$ of the determined monopole sources $\mathbf{x_{s,m}}$ of the real circular piston.

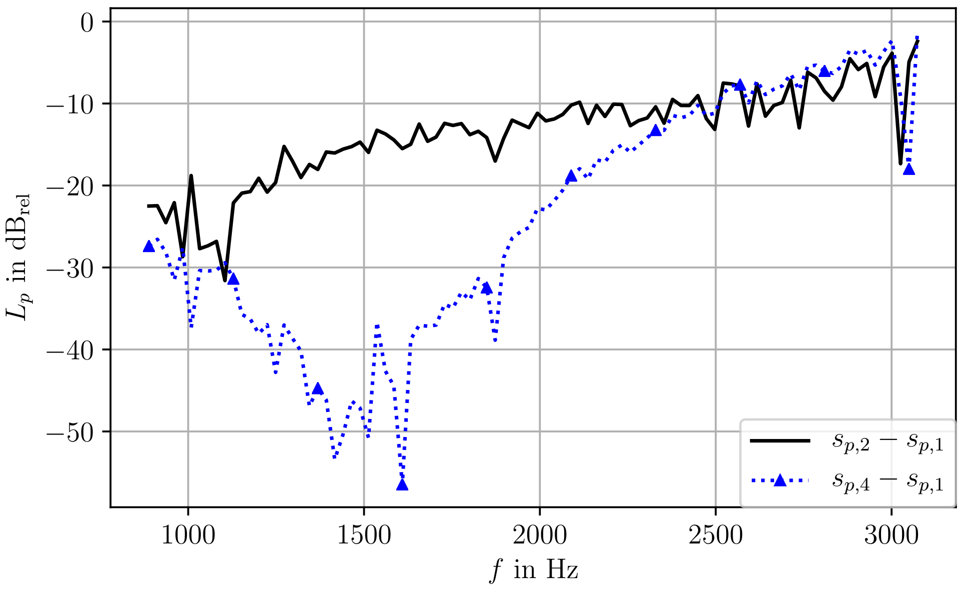

Fig. 21: Amplitude frequency response deviation of $s_{p,2}$ and $s_{p,4}$ to $s_{p,1}$.

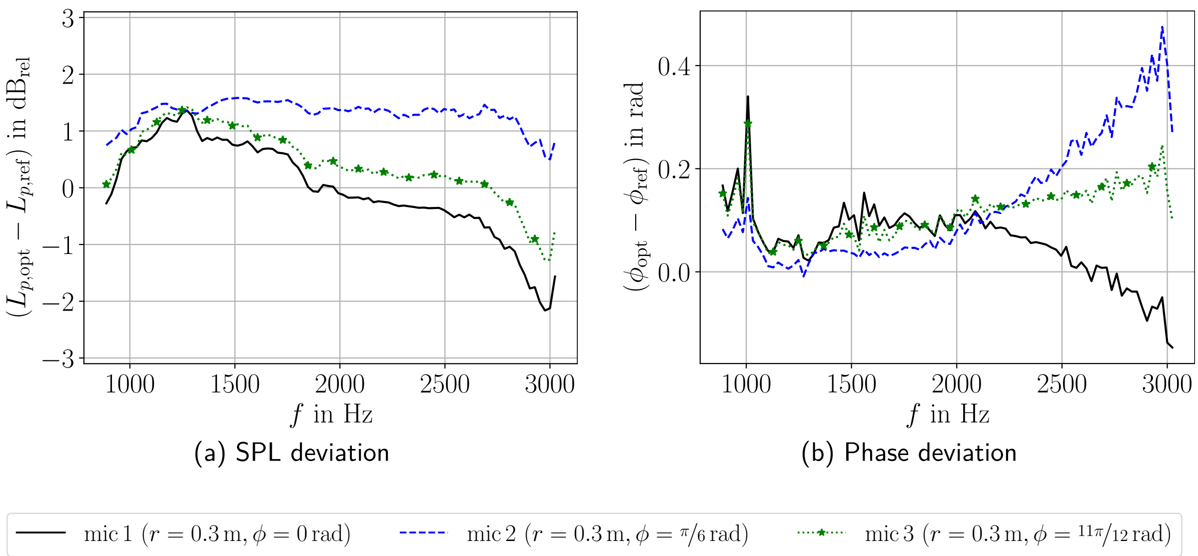

(a) SPL deviation

(b) Phase deviation

Fig. 22: SPL and phase deviation of the reference and optimized sound field at the virtual microphone positions of the circular piston ($K = 0.0$).

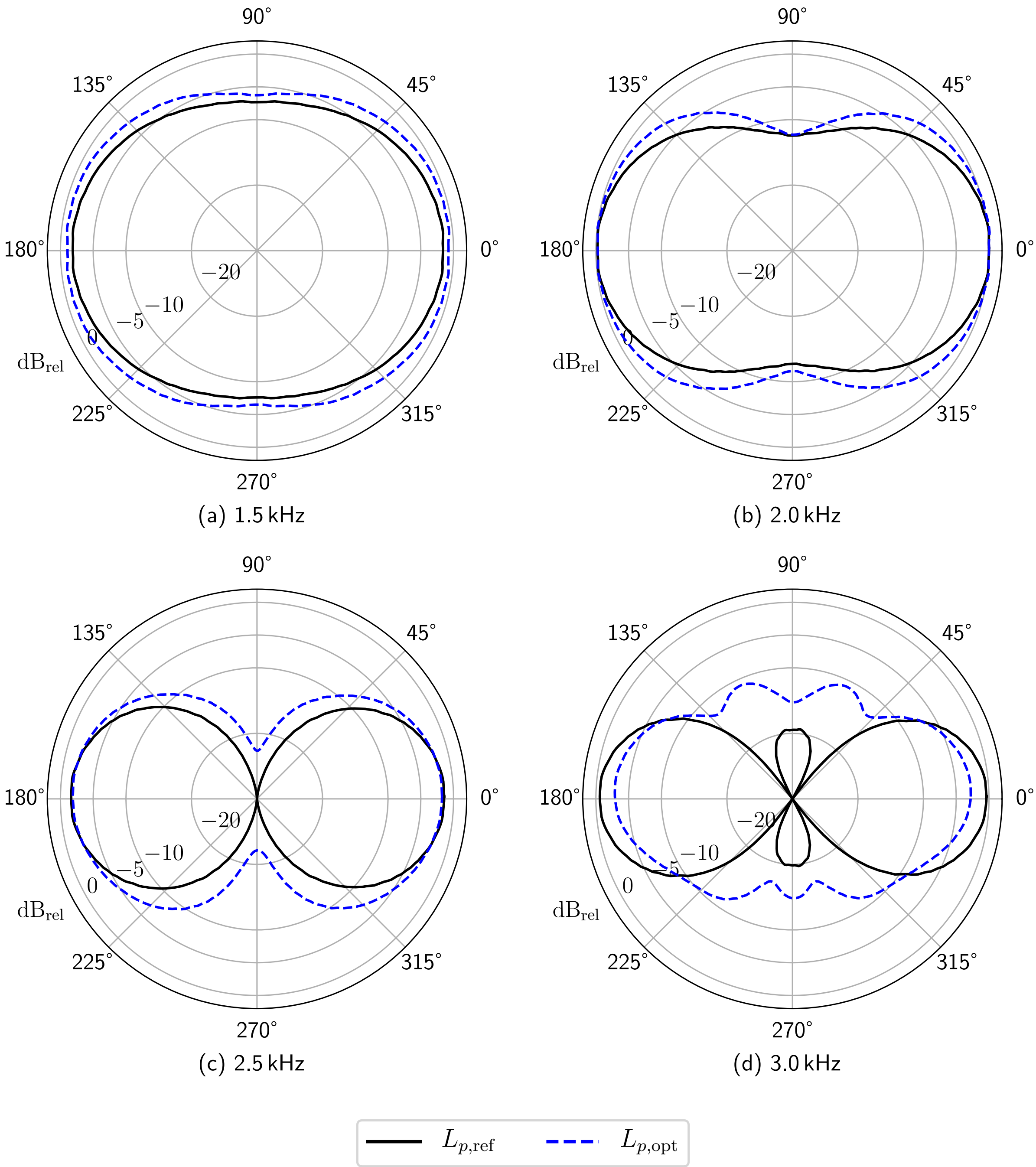

Fig. 23: Polar directivity patterns of the reference and optimized circular piston. The figures are taken at the circle radius $r = 0.3\,\mathrm{m}$ from the center of the source at $[0.5, 0.5, 0.5]^{\mathsf{T}}\,\mathrm{m}$ on the x_1-x_2-plane ($x_3 = 0.5\,\mathrm{m}$).

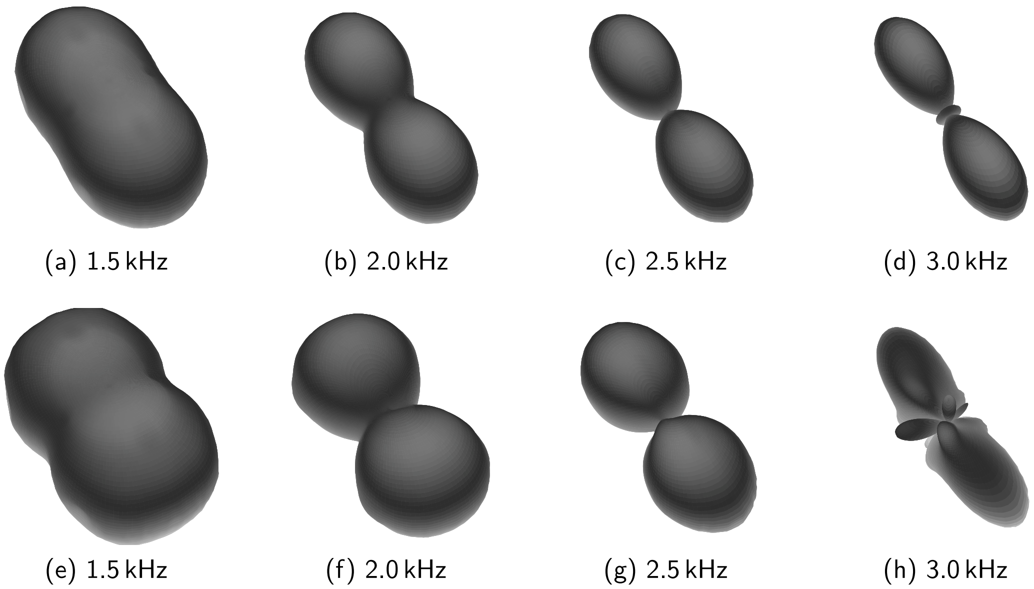

(a) 1.5 kHz (b) 2.0 kHz (c) 2.5 kHz (d) 3.0 kHz

(e) 1.5 kHz (f) 2.0 kHz (g) 2.5 kHz (h) 3.0 kHz

Fig. 24: Amplitude balloon plots of the reference (a-d) and optimized (e-h) circular piston sources. The plots are taken at the circle radius $r = 0.3$ m from the center of the source at $[0.5, 0.5, 0.5]^\mathsf{T}$ m.

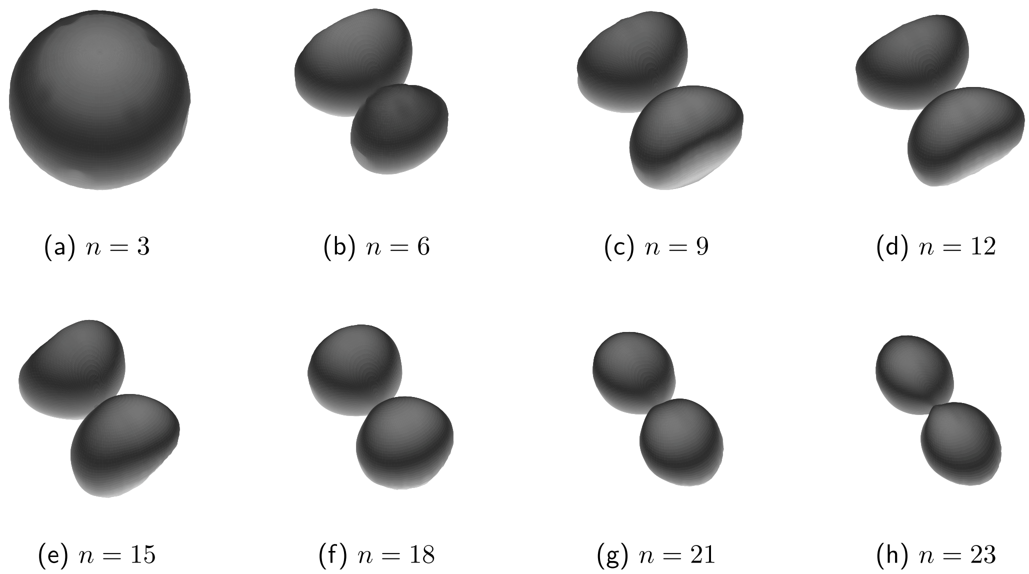

(a) $n = 3$ (b) $n = 6$ (c) $n = 9$ (d) $n = 12$

(e) $n = 15$ (f) $n = 18$ (g) $n = 21$ (h) $n = 23$

Fig. 25: Evolution process of the optimized circular piston at 2.5 kHz. The plots are taken at the circle radius $r = 0.3$ m from the center of the source at $[0.5, 0.5, 0.5]^\mathsf{T}$ m.

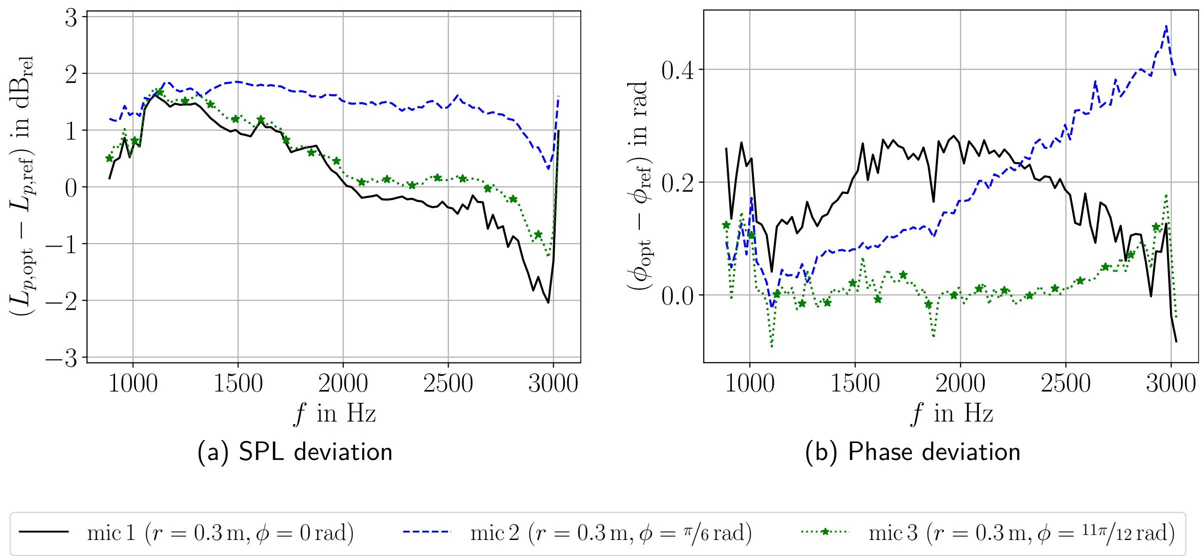

(a) SPL deviation

(b) Phase deviation

Fig. 26: SPL and phase deviation of the reference and optimized sound field at the virtual microphone positions of the complex circular piston with $K = 0.1$.

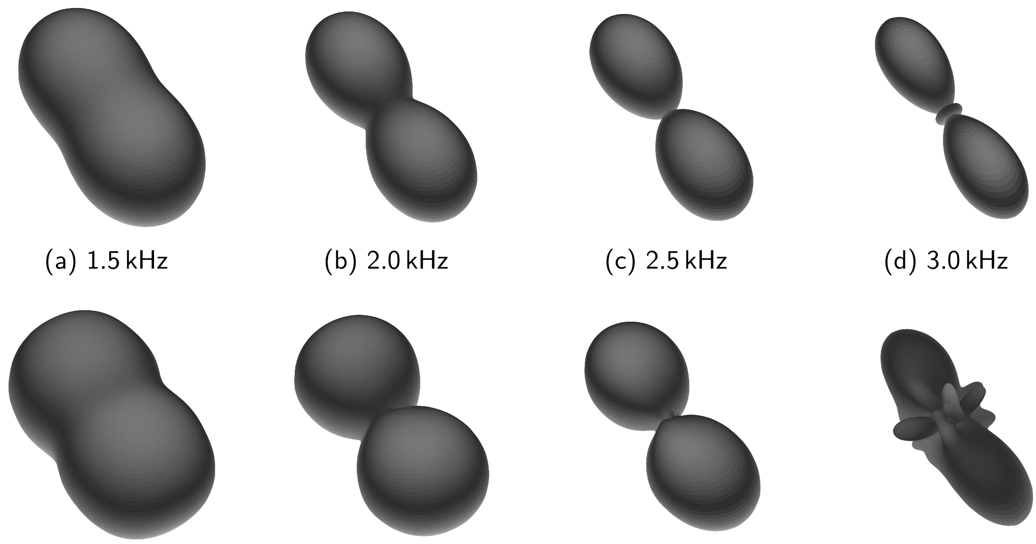

(a) 1.5 kHz (b) 2.0 kHz (c) 2.5 kHz (d) 3.0 kHz

(e) 1.5 kHz (f) 2.0 kHz (g) 2.5 kHz (h) 3.0 kHz

Fig. 27: Amplitude balloon plots of the reference (a-d) and optimized (e-h) complex circular piston with $K = 0.1$. The plots are taken at the circle radius $r = 0.3\,\mathrm{m}$ from the center of the source at $[0.5, 0.5, 0.5]^\mathsf{T}\,\mathrm{m}$.

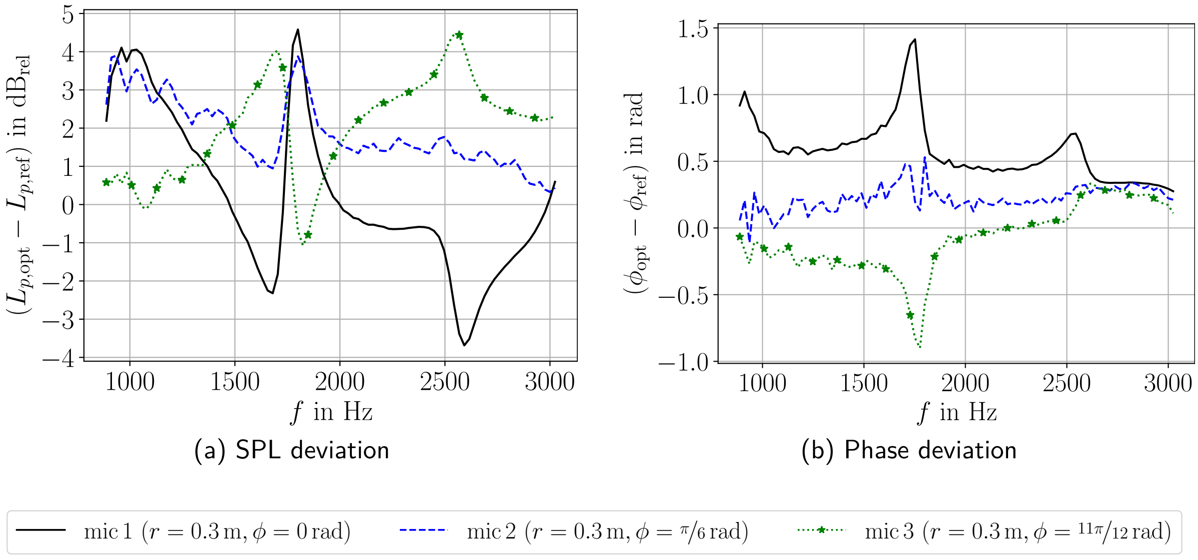

Fig. 28: SPL and phase deviation of the reference and optimized sound field at the virtual microphone positions of the complex circular piston with $K = 1.0$.

6 Conclusion

The present thesis introduced a novel method of monopole synthesis using an adjoint-based CAA solver in a finite differences time domain (FDTD) discretization scheme. In addition, a complex directivity point source (CDPS) solver in the frequency domain was implemented into the existing environment of the computational aeroacoustics (CAA) solver to efficiently compute reference sound fields as demonstrated in Sec. 5.1. Sec. 5.2 investigated the spatial expansion of the monopole sources. Following, the method was evaluated for a dipole, a quadrupole and a (complex) circular piston model.

In general, the method provided satisfactory results in the frequency range between 1.5 kHz and 2.5 kHz for the employed simulation setup. Also, it was demonstrated that the method is able to reproduce complex directivity patterns in the same manner as directivity patterns consisting only of real values. However, a higher complexity of the directive source in terms of amplitude and phase variations results in an inferior reproduction when the same amount of monopoles is used. It can be assumed that the correctly reproduced frequency range can be enlarged by (i) a larger computing domain, i.e., a larger spherical receiver radius to avoid near field shares on the evaluation sphere and (ii) a higher grid resolution, i.e., more grid nodes per meter in the computing domain to reduce the source expansion or increase the possible amount of monopole sources. A disadvantage of the method is that positioned monopole sources remain on their positions for the whole computation and a spatial adjustment is not possible.

The ability of the adjoint-based monopole synthesis method to reproduce sound sources with a high complexity, e.g., real world loudspeakers, was already demonstrated by Stein et al. (2020). Therein, the deviations are lower to the reference directivity pattern due to the variable location and the higher number of monopoles, or rather, Dirac pulses. In fact, the focus of this thesis was also to show how the adjoint-based monopole synthesis method proceeds to reproduce the directivity pattern. It principally locates monopoles around a main monopole in the center and transfers the forcing signal of the main monopole to the surrounding monopoles. Subsequently, the amplitude and the phase is adjusted. The presented method is also able to efficiently reproduce simple sources with a low number of monopoles, such as the dipole or the quadrupole. Moreover it was recognized that the objective function (see Fig. 29) begins to increase at a certain iteration loop due to the constant step width α_s at the line search process. To find a variable and optimized α_s, the Gaussian distribution has to be adjoint as well. This was not investigated since the grid-based method by Stein et al. (2020) provides more promising results.

In future, the method could be tested in a larger computing domain with a higher grid resolution (smaller $\Delta\mathbf{x}$) to reproduce a reference directivity pattern with greater precision and even synthesize very complex sources. As the available computing power is increasing rapidly in the recent time, more accurate calculations will be possible. A grid refinement of the source region—while the free space around the source region remain unrefined—could improve the directivity pattern reproduction as well.

References

Ahrens, J. (2012): *Analytic Methods of Sound Field Synthesis*. T-Labs Series in Telecommunication Services. Berlin, Heidelberg: Springer-Verlag.

Berkhout, A. J.; de Vries, D.; and Vogel, P. (1992): "Wave Front Synthesis: A New Direction in Electroacoustics." In: *Proc. of the 93rd Audio Eng. Soc. Conv.*

Bilbao, S.; Ahrens, J.; and Hamilton, B. (2019): "Incorporating Source Directivity in Wave-Based Virtual Acoustics: Time-Domain Models and Fitting to Measured Data." In: *The Journal of the Acoustical Society of America*, **146**(4), pp. 2692–2703.

Bilbao, S. and Hamilton, B. (2018): "Directional Sources in Wave-Based Acoustic Simulation." In: *IEEE/ACM Transactions on Audio, Speech, and Language Processing*, **27**(2), pp. 415–428.

Courant, R.; Friedrichs, K.; and Lewy, H. (1928): "Über die partiellen Differenzengleichungen der mathematischen Physik." In: *Mathematische Annalen*, **100**, pp. 32–74.

de Vries, D.; Start, E. W.; and Valstar, V. G. (1994): "The Wave Field Synthesis Concept Applied to Sound Reinforcement: Restrictions and Solutions." In: *Proc. of the 96th Audio Eng. Soc. Conv.*

Escolano, J.; Lopez, J.; and Pueo, B. (2007): "Directive Sources in Acoustic Discrete-Time Domain Simulations Based on Directivity Diagrams." In: *JASA Express Letters*, **121**, pp. 256–262.

Feistel, S.; Thompson, A.; and Ahnert, W. (2009): "Methods and Limitations of Line Source Simulation." In: *J. Audio Eng. Soc.*, **57**(6), pp. 379–402.

Gabriel, E.; et al. (2004): "Open MPI: Goals, Concept, and Design of a Next Generation MPI Implementation." In: *Proceedings, 11th European PVM/MPI Users' Group Meeting*. Budapest, Hungary, pp. 97–104.

Gaitonde, D. V. and Visbal, M. R. (2000): "Pade-Type Higher-Order Boundary Filter for the Navier-Stokes Equations." In: *AIAA Journal*, **38**, pp. 2103 – 2112.

Giles, M. B. and Pierce, N. A. (2000): "An Introduction to the Adjoint Approach to Design." In: *Flow, Turbulence and Combustion*, **65**(3), pp. 393–415.

Howe, M. S. (2002): *Theory of Vortex Sound*. Cambridge Texts in Applied Mathematics. Cambridge University Press.

Lele, S. K. (1992): "Compact Finite Difference Schemes with Spectral-Like Resolution." In: *Journal of Computational Physics*, **103**(1), pp. 16 – 42.

Lemke, M. (2015): *Adjoint Based Data Assimilation in Compressible Flows with Application to Pressure Determination from PIV Data*. Ph.D. thesis, Technische Universität Berlin.

Lemke, M.; Stein, L.; Hölter, A.; Straube, F.; and Weinzierl, S. (2020): "Synthese komplexer Richtcharakteristiken für eine Schallfeldoptimierung im Zeitbereich." In: *Fortschritte der Akustik: Tagungsband d. 46. DAGA*. pp. 1192–1195.

Mani, A. (2012): "Analysis and Optimization of Numerical Sponge Layers as a Nonreflective Boundary Treatment." In: *Journal of Computational Physics*, **231**(2), pp. 704–716.

Meyer, D. G. (1984): "Computer Simulation of Loudspeaker Directivity." In: *J. Audio Eng. Soc.*, **32**(5), pp. 294–315.

Meyer, P. and Schwenke, R. (2003): "Comparison of the Directional Point Source Model and BEM Model for Arrayed Loudspeakers." In: *Proc. of the Inst. of Acoustics*, **25**(4).

Möser, M. (2012): *Technische Akustik*. 9. Berlin, Heidelberg, New York: Springer.

Olver, F. W. J.; Lozier, D. W.; Boisvert, R. F.; and Clark, C. W. (2010): *NIST Handbook of Mathematical Functions*. 1. Cambridge University Press.

Opdam, R.; Latzke, K.; Behler, G.; and Vorländer, M. (2016): "Directivity as Monopole Decomposition for Active Noise Reduction." In: *Fortschritte der Akustik: Tagungsband d. 42. DAGA*. pp. 461–463.

Poinsot, T. J. and Lele, S. K. (1992): “Boundary Conditions for Direct Simulations of Compressible Viscous Flows.” In: *Journal of Computational Physics*, **101**(1), pp. 104 – 129.

Poirier-Quinot, D.; Katz, B.; and Noisternig, M. (2017): “EVERTims: Open Source Framework for Real-Time Auralization in Architectural Acoustics and Virtual Reality.” In: *Proc. of the 20th Int. Conf. on Digital Audio Effects*. pp. 323–328.

Redlich, J. (2017): *Zur Rekonstruktion gerichteter Schallquellen mittels Monopolsynthese*. Master’s thesis, Technische Universität Berlin.

Sakamoto, S. and Takahashi, R. (2013): “Directional Sound Source Modeling by Using Spherical Harmonic Functions for Finite-Difference Time-Domain Analysis.” In: *Proceedings of Meetings on Acoustics*, vol. 19. p. 015129.

Sarradj, E. (2016): *Kurzskript zur Vorlesung „Luftschall-Grundlagen“*. Technische Universität Berlin. Unpublished Lecture Notes.

Schultz, F.; Straube, F.; and Spors, S. (2015): “Discussion of the Wavefront Sculpture Technology Criteria for Straight Line Arrays.” In: *Proc. of the 138th Audio Eng. Soc. Conv., Warsaw*, #9323.

Sesterhenn, J. (2018): *Skript zur Vorlesung „Numerische Strömungsakustik“*. Technische Universität Berlin. Unpublished Lecture Notes.

Skudrzyk, E. (1971): *The Foundations of Acoustics*. New York: Springer.

Slavik, K. M. and Weinzierl, S. (2008): “Wiedergabeverfahren, 3D Audio.” In: Stefan Weinzierl (Ed.) *Handbuch der Audiotechnik*, chap. 11. Berlin, Heidelberg, New York: Springer, pp. 657–681.

Stein, L. (2019): *Simulation and Modeling of a Helmholtz Resonator under Grazing Turbulent Flow*. Ph.D. thesis, Technische Universität Berlin.

Stein, L.; Straube, F.; Sesterhenn, J.; Weinzierl, S.; and Lemke, M. (2019): "Adjoint-Based Optimization of Sound Reinforcement Including Non-Uniform Flow." In: *The Journal of the Acoustical Society of America*, **146**(3), pp. 1774–1785.

Stein, L.; Straube, F.; Weinzierl, S.; and Lemke, M. (2020): "Adjoint-Based FDTD Directional Sound Source Modeling Using Euler Equations." In: *The Journal of the Acoustical Society of America*. Submitted.

Straube, F. (2019): *Optimized Geometric and Electronic Wavefront Shaping with Line Source Arrays for Large-Scale Sound Reinforcement*. Ph.D. thesis, Technische Universität Berlin.

Takeuchi, D.; Yatabe, K.; and Oikawa, Y. (2019): "Source Directivity Approximation for Finite-Difference Time-Domain Simulation by Estimating Initial Value." In: *The Journal of the Acoustical Society of America*, **145**(4), pp. 2638–2649.

Tam, C. K. W. and Webb, J. C. (1993): "Dispersion-Relation-Preserving Finite Difference Schemes for Computational Acoustics." In: *Journal of Computational Physics*, **107**, pp. 262–281.

van Beuningen, G. W. J. and Start, E. W. (2000): "Optimizing Directivity Properties of DSP Controlled Loudspeaker Arrays." In: *Proc. of the Inst. of Acoustics: Reproduced Sound*, **22**(6), pp. 17–37.

Williams, E. G. (1999): *Fourier Acoustics – Sound Radiation and Nearfield Acoustical Holography*. Academic Press.

A Objective Functions and Source Positions

Fig. 29 shows the relative objective function J_n/J_0 over the iteration loop numbers n for the cases (III) - (V). The source positions $\mathbf{x_{s,m}}$ up to the minimum of J_n/J_0 are given in Tab. 4 and Tab. 5.

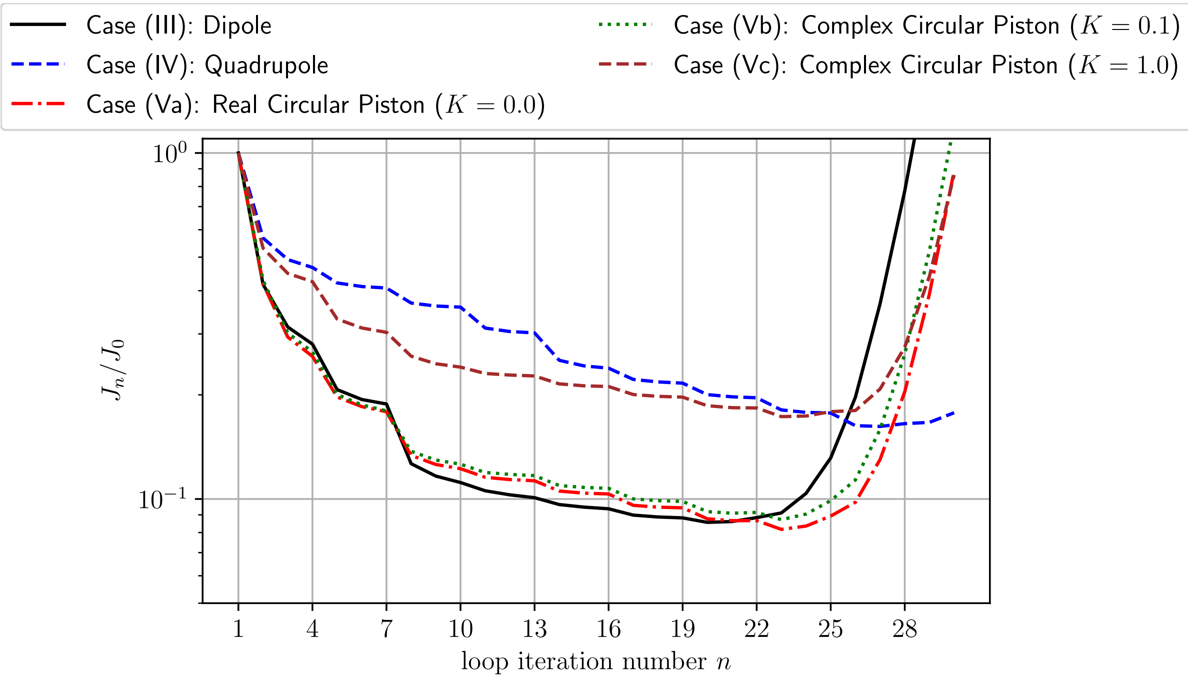

Fig. 29: Relative objective function J_n/J_0 over the iteration loops n. A new monopole source is added at every tick of the loop iteration number n.

Tab. 4: Monopole source positions of the cases (III) – (Va) determined by the adjoint-based monopole synthesis method.

Source	Case		
	(III): Dipole	(IV): Quadrupole	(Va): Circ. Piston ($K = 0.0$)
$\mathbf{x_{s,1}}$ in m	$[0.50, 0.50, 0.50]^\mathsf{T}$	$[0.50, 0.50, 0.50]^\mathsf{T}$	$[0.46, 0.50, 0.50]^\mathsf{T}$
$\mathbf{x_{s,2}}$ in m	$[0.42, 0.50, 0.50]^\mathsf{T}$	$[0.57, 0.57, 0.50]^\mathsf{T}$	$[0.42, 0.50, 0.50]^\mathsf{T}$
$\mathbf{x_{s,3}}$ in m	$[0.59, 0.50, 0.51]^\mathsf{T}$	$[0.44, 0.44, 0.50]^\mathsf{T}$	$[0.59, 0.50, 0.51]^\mathsf{T}$
$\mathbf{x_{s,4}}$ in m	$[0.50, 0.50, 0.42]^\mathsf{T}$	$[0.44, 0.57, 0.50]^\mathsf{T}$	$[0.50, 0.50, 0.42]^\mathsf{T}$
$\mathbf{x_{s,5}}$ in m	$[0.50, 0.58, 0.46]^\mathsf{T}$	$[0.57, 0.44, 0.50]^\mathsf{T}$	$[0.50, 0.58, 0.46]^\mathsf{T}$
$\mathbf{x_{s,6}}$ in m	$[0.50, 0.42, 0.46]^\mathsf{T}$	$[0.50, 0.65, 0.50]^\mathsf{T}$	$[0.50, 0.42, 0.46]^\mathsf{T}$
$\mathbf{x_{s,7}}$ in m	$[0.50, 0.58, 0.55]^\mathsf{T}$	$[0.50, 0.38, 0.50]^\mathsf{T}$	$[0.50, 0.57, 0.56]^\mathsf{T}$
$\mathbf{x_{s,8}}$ in m	–	$[0.63, 0.50, 0.50]^\mathsf{T}$	$[0.50, 0.49, 0.59]^\mathsf{T}$
$\mathbf{x_{s,9}}$ in m	–	$[0.38, 0.50, 0.50]^\mathsf{T}$	–

Tab. 5: Monopole source positions of the cases (Vb) – (Vc) determined by the adjoint-based monopole synthesis method.

Source	Case	
	(Vb): Cmp. Circ. Piston ($K = 0.1$)	(Vc): Cmp. Circ. Piston ($K = 1.0$)
$\mathbf{x_{s,1}}$ in m	$[0.50, 0.50, 0.50]^\mathsf{T}$	$[0.47, 0.50, 0.50]^\mathsf{T}$
$\mathbf{x_{s,2}}$ in m	$[0.59, 0.50, 0.51]^\mathsf{T}$	$[0.38, 0.50, 0.50]^\mathsf{T}$
$\mathbf{x_{s,3}}$ in m	$[0.42, 0.50, 0.50]^\mathsf{T}$	$[0.58, 0.50, 0.50]^\mathsf{T}$
$\mathbf{x_{s,4}}$ in m	$[0.50, 0.50, 0.42]^\mathsf{T}$	$[0.48, 0.57, 0.59]^\mathsf{T}$
$\mathbf{x_{s,5}}$ in m	$[0.50, 0.58, 0.46]^\mathsf{T}$	$[0.48, 0.58, 0.54]^\mathsf{T}$
$\mathbf{x_{s,6}}$ in m	$[0.50, 0.42, 0.46]^\mathsf{T}$	$[0.49, 0.57, 0.46]^\mathsf{T}$
$\mathbf{x_{s,7}}$ in m	$[0.50, 0.57, 0.56]^\mathsf{T}$	$[0.48, 0.43, 0.54]^\mathsf{T}$
$\mathbf{x_{s,8}}$ in m	$[0.50, 0.49, 0.59]^\mathsf{T}$	$[0.48, 0.50, 0.42]^\mathsf{T}$